

Secondary reactions of aromatics-derived oxygenated organic molecules lead to plentiful highly oxygenated organic molecules within an intraday OH exposure

Yuwei Wang¹, Chuang Li¹, Ying Zhang¹, Yueyang Li¹, Gan Yang¹, Xueyan Yang¹, Yizhen Wu¹, Lei Yao^{1,2}, Hefeng Zhang^{3*}, Lin Wang^{1,2,4,5,6*}

¹ Shanghai Key Laboratory of Atmospheric Particle Pollution and Prevention (LAP³), Department of Environmental Science and Engineering, Jiangwan Campus, Fudan University, Shanghai 200438, China

² Shanghai Institute of Pollution Control and Ecological Security, Shanghai 200092, China

³ State Environmental Protection Key Laboratory of Vehicle Emission Control and Simulation, Vehicle Emission Control Center of Ministry of Ecology and Environment, Chinese Research Academy of Environmental Sciences, Beijing 100012, China

⁴ IRDR International Center of Excellence on Risk Interconnectivity and Governance on Weather/Climate Extremes Impact and Public Health, Fudan University

⁵ National Observations and Research Station for Wetland Ecosystems of the Yangtze Estuary, Shanghai, China

⁶ Collaborative Innovation Center of Climate Change, Nanjing, 210023, China

* Corresponding Author: H.Z., email, zhanghf@craes.org.cn; phone, +86-10-84915586

L.W., email, lin_wang@fudan.edu.cn; phone, +86-21-31243568

ABSTRACT. Highly oxygenated organic molecules (HOMs) can participate in new particle formation (NPF) and enhance growth of newly formed particles partially because of their low volatility. Previous studies have shown formation of HOMs via autoxidation reactions of RO₂ intermediates generated by OH-initiated oxidation of anthropogenic volatile organic compounds (VOCs). It was also suggested that multi-generation OH oxidation could be an important source for aromatics-derived HOMs. However, our understanding on the generation of aromatics-derived HOMs are still insufficient, especially for their formation mechanisms, which determine molar yields of HOMs and are essential to the establishment of global chemical box models related to HOMs. In this study, with a potential aerosol ~~massformation~~ oxidation flow reactor (PAM OFR), two series of OH-initiated oxidation experiments of 1,3,5-trimethylbenzene (1,3,5-TMB) were conducted to investigate the formation of aromatics-derived HOMs. In the first series, the evolution of oxidation products of 1,3,5-TMB in an OH exposure range of $(0.5 - 5.0) \times 10^{10}$ molecules cm⁻³ s, equivalent to an OH exposure of 0.7 – 6.9 hours at an OH concentration ([OH]) of 2×10^6 molecules cm⁻³, was investigated by a nitrate-based chemical ionization mass spectrometer and a Vocus proton-transfer-reaction mass spectrometer, indicating significant secondary OH chemistry during the ageing of stabilized

37 first generation oxygenated products within an intraday OH exposure and formation of various
38 HOMs with lower double bond equivalence (DBE). In addition, organonitrates, formed after
39 the introduction of NO_x into the reaction systems, further confirmed the existence of such
40 secondary reactions. The second series of experiments was conducted with same residence time
41 but much lower [OH], which also shows the generation of multi-generation HOMs with an [OH]
42 as low as 1.06×10⁷ molecules cm⁻³ for 53 s, i.e., an OH exposure of around 5.86×10⁸ molecules
43 cm⁻³ s. Our study suggests an important role of secondary OH chemistry in the oxidation of
44 aromatics, if these oxygenated products survived long enough in the ambient, and elucidates
45 detailed formation mechanisms of certain HOM products.

46 **1 Introduction**

47 OH radicals can react with volatile organic compounds (VOCs) in the atmosphere,
48 converting primary pollutants to secondary ones. Generated from oxidation of VOCs,
49 oxygenated organic molecules (OOMs) are crucial in a variety of atmospheric chemical
50 processes, contributing efficiently to the formation of secondary organic aerosols (SOAs) and
51 ground-level O₃ (Ng et al., 2010; Wang et al., 2022; Qu et al., 2021). Among the enormous
52 number of oxygenated VOCs (OVOCs), highly oxygenated organic molecules (HOMs) have
53 recently attracted significant attention (Bianchi et al., 2019). Most of HOMs are low volatility
54 organic compounds (LVOCs) or extremely low volatility organic compounds (ELVOCs), and
55 thus are able to drive the initial formation of nucleated particles under certain conditions and
56 contribute to the subsequent growth of newly-formed particles, which finally enhance SOA
57 formation (Tröstl et al., 2016; Lehtipalo et al., 2018; Stolzenburg et al., 2018; Mohr et al., 2019;
58 Qiao et al., 2021).

59 Formation of HOMs is ~~typically~~ triggered by oxidation of VOCs in the gas phase. Peroxy
60 radicals (RO₂) are generated at the initial step and will undergo an intramolecular hydrogen
61 atom shift forming a hydroperoxide functionality and an alkyl radical. A molecular oxygen will
62 rapidly attach to this alkyl radical and form a new and more oxidized RO₂. This reaction is
63 called as autoxidation and the newly formed RO₂ can go through another autoxidation or
64 bimolecular termination reactions to form a stabilized product (Crouse et al., 2013).
65 Autoxidation is suggested to be responsible for widely detected HOMs in the atmosphere,
66 because it can form highly oxygenated RO₂ in a short time scale. In terms of bimolecular
67 reactions, RO₂ reacts appreciable only with hydroperoxyl radical (HO₂), NO, and another RO₂.
68 The RO₂ reaction chain in polluted areas is largely terminated by NO, which prohibits
69 generation of compounds with high oxidation levels and reduces yields of HOMs (Bianchi et
70 al., 2019).

71 Nevertheless, autoxidation reactions alone are not enough to explain the large numbers of
72 oxygen atoms and low double bond equivalence (DBE, calculated as $nC - \frac{nH+nN}{2} + 1$ where
73 nC , nH , and nN stand for the number of ~~containing~~-carbon, hydrogen, and nitrogen atoms,
74 respectively, in a molecular) ~~in-for~~ HOMs observed in laboratory experiments and ambient
75 campaigns. Take alkylbenzenes as an example, previous studies suggest that the main products
76 of OH-initiated oxidation of alkylbenzenes (C_xH_{2x-6} , $x=7, 8, \text{ or } 9$), i.e., bicyclic peroxy radicals
77 (BPR, $C_xH_{2x-56}O_5^*$, $x=7, 8, \text{ or } 9$) (Jenkin et al., 2003), can undergo an autoxidation reaction and
78 form a new peroxy radical, $C_xH_{2x-56}O_7^*$ ($x=7, 8, \text{ or } 9$) (Wang et al., 2017). ~~The a~~Autoxidation of
79 BPR could be very fast if it has a favorable structure, as found in a previous study (Wang et al.,
80 2017). On the other hand, the structure of the resulting $C_xH_{2x-56}O_7^*$ is strongly different from
81 that of BPR, whose autoxidation reaction rate can be as low as the order of 0.001 s^{-1} , since it
82 lacks enhancements from favorable transition state geometries and substitutes or resonance
83 structures (Bianchi et al., 2019; Otkjær et al., 2018). Such a slow autoxidation reaction rate
84 cannot explain the extensive existence of HOM monomers with more than 7 oxygen atoms and
85 HOM dimers with more than 10 oxygen atoms, which are the maximum numbers of oxygen
86 atoms in stabilized first generation monomer and dimer products, respectively, formed from
87 $C_xH_{2x-56}O_7^*$ (Molteni et al., 2018; Wang et al., 2020b; Mentel et al., 2015; Berndt et al., 2018b).
88 Another possibility is the formation of a second oxygen bridge after the hydrogen shift of BPR
89 (Molteni et al., 2018), but this reaction pathway would not allow a further oxygenation reaction
90 without a breakage of the carbon ring, which is also unpromising. A very recent investigation
91 offers new insights into the formation mechanism of these products, indicating the molecular
92 rearrangement of BPR can initiate a series of autoxidation (Iyer et al., 2023). However, the
93 formation mechanism of HOMs with a large hydrogen atom number, i.e., low DBE, is still
94 vague. For example, monomer products with 16 hydrogen atoms in the OH-initiated oxidation
95 of TMB and those with 14 hydrogen atoms in the OH-initiated oxidation of xylene were
96 observed in the laboratory, both with a DBE of 2 lower than their precursors' (Molteni et al.,
97 2018), but their formation mechanisms cannot be explained by any known mechanisms with
98 only one OH attack.

99 Multigeneration reactions of VOCs complicate HOMs' formation. Previous studies
100 indicate that HOMs can also be formed by sequential oxidation of stabilized first-generation
101 products of benzene and toluene (Garmash et al., 2020; Cheng et al., 2021). Garmash et al.
102 (2020) conducted OH oxidation experiments of benzene and toluene with an OH exposure
103 equivalent to atmospheric oxidation times of 10 hours – 15 days at OH concentrations of $\sim 10^6$
104 molecules cm^{-3} . Cheng et al. (2021) simulated oxidation of benzene and toluene with an OH
105 exposure equivalent to 2.4 – 19.4 days of atmospheric photochemical ageing. Certainly, such

106 extremely high OH exposures favor secondary OH chemistry and help to facilitate our
107 understanding on product distributions, but such a long timescale limits atmospheric
108 implications of their results, given the complex physical and chemical processes that occur at
109 night.

110 Compared to benzene and toluene, trimethylbenzene (TMB) is a ~~compound precursor~~
111 characterized with much larger HOM molar yields when reacted with OH, and the abundance
112 of TMB in the atmosphere is unignorable (Molteni et al., 2018; Yuan et al., 2012). Previous
113 laboratory experiments on TMB-derived HOMs mainly focused on the autoxidation reactions
114 of BPR and the influences of NO_x, ~~while~~ and the quantity of experiments was very finite,
115 restricting the application of their conclusions to ~~the more~~ atmospheric relevant conditions
116 (Tsiligiannis et al., 2019; Wang et al., 2020b). From the mechanism perspective, a number of
117 HOM monomers with more than 7 oxygen atoms detected in the OH-initiated oxidation of
118 TMB were previously assumed to be generated via multiple autoxidation reactions (Molteni et
119 al., 2018). Nevertheless, a subsequent OH oxidation of the first-generation oxygenated products
120 might be more plausible for the formation of HOM monomers with more than 7 oxygen atoms
121 from the present point of view. Indeed, laboratory experiments show that RO₂ formed during
122 the second-generation OH oxidation of the stabilized first-generation ~~stabilized~~ oxidation
123 products can also undergo autoxidation reactions, which entangles reaction mechanisms
124 potentially involved in the formation of those HOMs and justifies more investigations on the
125 multigeneration OH oxidation of aromatics (Wang et al., 2020b). Atmospheric OH ~~with an~~
126 atmospheric concentration ([OH]) up to $6 \times 10^6 - 2.6 \times 10^7$ molecule cm⁻³, which is several times
127 higher than the typical average atmospheric [OH], 1.5×10^6 molecule cm⁻³ (Jacob, 1999), has
128 been frequently observed in both urban and suburban environments in China (Tan et al., 2019;
129 Lu et al., 2012), leading to a realistic implication of multigeneration OH oxidation. Therefore,
130 it is imperative to study chemical characteristics of ~~formation reactions of aromatics-derived~~
131 HOMs at different OH exposures, especially those that are fewer less than or equivalent to one
132 day of atmospheric oxidation.

133 In this study, ~~a two~~ series of laboratory experiments ~~were conducted on the~~ OH-initiated
134 oxidation of 1,3,5-TMB, selected as an example of anthropogenic VOCs, ~~were conducted. One~~
135 was conducted with [OH] ~~as high as ranging from~~ 9.32×10^7 ~~to~~ 1.03×10^9 molecule cm⁻³ ~~and,~~
136 corresponding to an OH exposure equivalent to atmospheric oxidation times of roughly 0.7 –
137 6.9 hours at an average daytime [OH] of 2.0×10^6 molecules cm⁻³. A nitrate-based chemical
138 ionization mass spectrometer (nitrate CIMS) and a Vocus proton-transfer-reaction mass
139 spectrometer (Vocus PTR) were deployed to measure the oxidation products and the precursor,
140 respectively. ~~From the evolution of oxygenated products, w~~ We explored the evolution of

141 ~~oxidation products to investigate the~~ secondary OH chemistry of stabilized first-generation
142 ~~oxygenated oxidation~~ products generated by the oxidation of 1,3,5-TMB. Furthermore, the
143 influence of NO on the formation of HOMs was investigated by introducing N₂O into the
144 reaction system ~~via formation of organonitrates~~. In addition, another series of experiments
145 under atmospheric relevant [OH] were conducted to confirm the applicability of the above-
146 developed multi-generation OH oxidation mechanisms in the ambient atmosphere.

147 2 Methods

148 OH-initiated oxidation of 1,3,5-TMB was investigated in a potential aerosol
149 ~~massformation~~ oxidation flow reactor (PAM OFR) system at $T = 298 \pm 1$ K and a pressure of
150 1 atm (Lambe et al., 2015). Two series of experiments were conducted, one under high [OH]
151 conditions and the other under low [OH] conditions. Hereafter, we refer to the series of high
152 [OH] experiments as ‘the 1st-round experiments’ and the low [OH] ~~ones~~ as ‘the 2nd-round
153 experiments’, respectively. The i^{th} experiment in the 1st-round experiments is labelled as 1- i and
154 the one in the 2nd-round experiments as 2- i , where i stands for its serial number. The
155 experimental settings in this study differed slightly from what were used previously (Wang et
156 al., 2020b). In the 1st-round experiments, forty OH experiments without NO_x (Exp. 1-1 – 1-40)
157 and twenty-eight experiments with NO_x (Exp. 1-41 – 1-68) were performed. Seven experiments
158 were conducted in the 2nd-round, four without NO_x ([Exp. 2-1 – 2-4](#)) and three with NO_x ([Exp.](#)
159 [2-5 – 2-7](#)). The experimental conditions are summarized in [Table S1](#), including concentrations
160 of the precursor, ozone, and NO and NO₂. The equivalent OH exposure in the OFR for each
161 experiment was estimated according to the precursor consumption, [and](#) also listed in [Table S1](#).
162 OH exposures in the OFR were in the range of $(5.2 - 48.7) \times 10^9$ and $(0.6 - 5.5) \times 10^9$ molecules
163 cm⁻³ s in the 1st-round and 2nd-round experiments, respectively.

164 A home-made 1,3,5-TMB/N₂ cylinder was used as a stable gaseous precursor source in the
165 experiments, from which the flow rate of 1,3,5-TMB/N₂ varied between 1 – 3 sccm (standard
166 cubic centimeter per minute, ~~standard to 0 °C, 1 atm~~), leading to ~~$7.08 \times 10^{11} 28.9 - 1.54 \times 10^{12} 62.7$~~
167 ~~molecule cm⁻³ ppb~~ of 1,3,5-TMB in the 1st-round experiments, and ~~$-7.55 \times 10^{11} 30.8$~~ or
168 ~~$8.45 \times 10^{11} 34.5$~~ molecule cm⁻³ ppb of 1,3,5-TMB in the 2nd-round experiments, respectively
169 ([Table S1](#)). A total flow of 15 slpm (standard liters per minute, ~~standard to 0 °C, 1 atm~~) zero-
170 gas generated by a zero-gas generator (model 737-13, Aadco Instruments Inc.), together with
171 the 1,3,5-TMB/N₂ flow, was introduced into the OFR. The reaction time in both series of
172 experiments was kept at around 53 s and the flow reactor was kept as a plug flow ~~one~~ in both
173 series. The flow in the PAM OFR is laminar with a very low axial mixing, as characterized
174 with a Taylor dispersion model in a previous study (Lambe et al., 2011). ~~Among the 15 slpm~~

175 ~~zero-gas~~, 6 slpm out of the 15 slpm zero-gas was initially passed through a Nafion humidifier
176 (Perma Pure Model FC100-80-6MSS) filled with ultra-pure water and finally converged with
177 the main flow into the OFR to achieve and keep a desired RH of 20.0 ± 2.5 % in the OFR
178 throughout all the experiments, and 2 slpm was initially passed through a separate ozone
179 chamber, resulting in an initial ozone concentration of around ~~429~~ 1.05×10^{13} – ~~881~~ 2.16×10^{13}
180 molecule cm⁻³ ppb in the OFR in the 1st-round experiments and ~~123~~ 3.01×10^{12} – ~~1523.72~~ 10^{12}
181 molecule cm⁻³ ppb in the 2nd-round experiments, respectively. The OFR was operated with only
182 the 254 nm lights on, under which the primary oxidant production reactions in the OFR were
183 $O_3 + hv (254 \text{ nm}) \rightarrow O_2 + O(^1D)$ and $O(^1D) + H_2O \rightarrow 2OH$. After turning on of UV lights,
184 a ~~certain~~-HOM compound is believed to be generated if its signal is more than 3 standard
185 deviations of its background signal. If the fluctuations in the 1-min-averaged signals of both
186 TMB in the Vocus PTR and typical HOMs (i.e., C₉H₁₄O₇(NO₃)) in the nitrate CIMS are within
187 2% during a 10-min period, ~~we assume that~~ a steady state ~~has been~~ was assumed to be reached.
188 It usually took around no more than 2 minutes for the signals of HOMs to stabilize after the
189 adjustment of UV lights. We typically monitored the reaction products for around 20 minutes
190 for each experiment. An ozone monitor (Model 106-M, 2B technologies) and a trace-gas
191 analyzer for NO-NO₂-NO_x (Thermo, 42i-TL) were placed at the exit of the OFR to measure
192 concentrations of ozone and NO_x, respectively.

193 Non-tropospheric VOC and OVOC photolysis is a typical issue that should be taken into
194 account when evaluating the OFR settings of OFR laboratory experiments, especially under the
195 high UV light dose settings in the 1st-round experiments. Our evaluation on P photolysis of the
196 precursor and HOMs ~~shows were evaluated, showing~~ that photolysis was not a contributor to
197 our observation on C9 and C18 HOM formation. The photolysis rate of 1,3,5-TMB can be
198 estimated based on the absorption cross-sections of 1,3,5-TMB at 254 nm (Keller-Rudek et al.,
199 2013) and UV photon fluxes estimated by a chemistry model discussed in the following sections.
200 The ratio of photolysis-to-OH reaction for 1,3,5-TMB in our 1st-round experiments was merely
201 0.010 – 0.033. Hence, photolysis of 1,3,5-TMB was insignificant in the OFR. For stabilized
202 products such as C9 and C18 HOMs, the cross sections of organic molecules are usually ~
203 3.9×10^{-18} – 3.9×10^{-17} cm² (Peng et al., 2016), while the reaction rate between OH and the
204 stabilized first-generation products are estimated to be around 1.28×10^{-10} molecule⁻¹ cm³ s⁻¹, as
205 suggested by Master Chemical Mechanism (MCM) (Jenkin et al., 2003). Hence, the ratio of
206 photolysis rates of C9 and C18 HOMs to their secondary OH oxidation rates is estimated to be
207 ~~merely~~ around 0.020 – 0.056 in the 1st-round experiments. In the 2nd-round, the influences of
208 photolysis should be even lower due to the much lower light intensity.

209 For experiments with NO_x in the 1st-round experiments, 350 sccm N₂O (99.999%, Air
 210 Liquid) was added into the OFR to produce and sustain NO_x mixing ratios at levels that were
 211 sufficiently high to be a competitive sink for RO₂ radicals. NO and NO₂ were produced via the
 212 reaction $N_2O + O(^1D) \rightarrow 2NO$, followed by the reaction $NO + O_3 \rightarrow NO_2 + O_2$. Two sets of
 213 irradiance intensities were chosen for NO_x experiments, generally resulting in two NO_x levels,
 214 ~~1.84.41×10¹⁰ ppb molecule cm⁻³~~ NO + ~~70-1.72×10¹² molecule cm⁻³ppb~~ NO₂ (Exp. 1-41 – 1-54)
 215 and ~~1.18×10¹¹ molecule cm⁻³4.8 ppb~~ NO + ~~2.94×10¹² molecule cm⁻³120 ppb~~ NO₂ (Exp. 1-55 –
 216 1-68) at the exit of the OFR. With the aim to slightly modify OH exposure but keep NO_x
 217 concentrations constant among each set of experiments, the initial concentrations of 1,3,5-TMB
 218 were adjusted in a large range ~~from (4.09×10¹¹46.7~~ ~~to 2.06×10¹²84.1 molecule cm⁻³ppb)~~
 219 ~~while RH and irradiances were not changed~~, as an increase in the precursor concentration
 220 corresponds to a larger sink for OH, ~~while RH and irradiances were not changed~~. In the 2nd-
 221 round experiments, due to the lower ~~(O¹D)~~ in the PAM OFR, 2.5 slpm pure N₂O was utilized
 222 instead, whereas the total flow rate was kept the same as that in the 1st-round. We lowered the
 223 light intensity to obtain a lower [OH] in the PAM OFR, which also resulted in fluctuations in
 224 the NO concentrations ([NO]) from ~~3.19×10¹⁰4.3~~ to ~~1.74×10¹¹7.1 molecule cm⁻³ppb~~ and the
 225 NO₂ concentrations ([NO₂]) from ~~2.70×10¹¹41~~ to ~~9.31×10¹¹38 molecule cm⁻³ppb~~.

226 A nitrate CIMS (Ehn et al., 2014; Eisele and Tanner, 1993) and a Vocus PTR (Krechmer
 227 et al., 2018) were deployed at the exit of the OFR to measure the oxidation products of 1,3,5-
 228 TMB in the 1st-round experiments. These two mass spectrometers have been well characterized
 229 in a previous study (Wang et al., 2020b).

230 The sample flow rate for the nitrate CIMS in the 1st round-experiments was 8 slpm through
 231 a Teflon tube with an outer diameter (OD) of 1/4 in. and a length of 70 cm. The sheath flow for
 232 the nitrate CIMS was supplied by a zero-gas generator at a flow rate of 15 slpm. Mass resolution
 233 was approximately 8000 for ions with m/z larger than 200 Th. HOMs generated from TMB
 234 oxidation were charged in the ambient pressure interface region by collisions with nitrate
 235 clusters, (HNO₃)_x·NO₃⁻ (x = 0 – 2), and detected by nitrate CIMS as clusters with NO₃⁻, i.e.,
 236 HOM·NO₃⁻ (Hyytinen et al., 2015). In addition, HOMs' signals were corrected with relative
 237 transmission efficiencies of our nitrate CIMS ~~obtained via a method reported previously~~
 238 (Heinritzi et al., 2016). We followed the same sampling method of PAM OFR as those in
 239 previous studies, in order to obtain a similar flow tube residence time distributions (RTDs) and
 240 thus validate usage of a modified PAM_chem_v8 model to estimate concentrations of radicals
 241 in the OFR as discussed below. ~~We acknowledge that this is not a perfect sampling setting for~~
 242 ~~nitrate CIMS. However, the reduction in the sampling efficiencies of various HOMs is likely~~
 243 ~~to be close, if not identical, which keeps the distributions of HOMs.~~

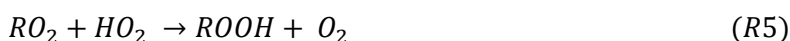
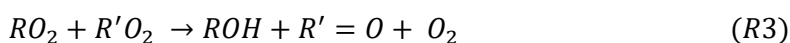
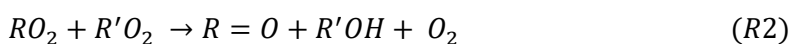
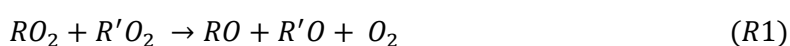
244 Vocus PTR was applied to quantify precursor concentrations ~~and measure volatile and~~
245 ~~intermediate volatility oxidation products~~. The focusing ion-molecule reactor (FIMR) was
246 heated up and its temperature was maintained at 100 °C during the experiments. The FIMR can
247 be operated under 2.0 mbar without a strong interference from corresponding water clusters
248 when ionizing the neutral compounds. The Vocus front and back voltages were 650 V and 15
249 V, respectively, forming an axial voltage of 635V and a reduced electrical field (E/N , where E
250 is the electric field strength and N is the number density of the buffer gas in FIMR) of 180 Td.
251 The radio frequency (RF) voltages and frequency were set to be 450 V and 1.3 MHz,
252 respectively. The sample flow was introduced to the Vocus PTR through a Teflon tube with an
253 OD of 1/4 in. and a length of 120 cm from the OFR. A total sample flow of 1.4 slpm was
254 maintained by a pump with an orifice to minimize the delay time of sampling, from which
255 approximately 125 sccm was sampled into the FIMR through a capillary tube.

256 In the 2nd-round experiments, a Vocus CI-TOF (Towerk AG, Switzerland) equipped with
257 a Vocus Aim inlet and the same nitrate-ion chemical ionization source as adopted in the 1st-
258 round experiments was utilized to measure oxidation products, hereafter referred as nitrate CI-
259 TOF. The nitrate CI-TOF was characterized with a flat transmission efficiency between m/z 60
260 Th and m/z 500 Th, as well as a mass resolution of 10000 at m/z 200 Th. In this series of
261 experiments, the reaction products were sampled from the PAM OFR via a 30 cm-long Teflon
262 tube with a 1/2 in. OD to our nitrate CI-TOF. The Vocus PTR and the ozone monitor were
263 connected to the PAM OFR from a separate port via a 120 cm-long Teflon tube with a 1/4 in.
264 OD.

265 We did not quantify HOMs' concentrations. Since the inner diameters of PAM OFR,
266 sampling tube, and the nitrate CIMS inlet were different, and two reducing unions were used
267 during sampling, the estimation of the penetration efficiency and sampling efficiency of HOMs
268 are thus of a significant uncertainty. The initial concentrations of TMB utilized in both sets of
269 experiments fluctuated slightly, which resulted from sample preparation processes and were
270 more obvious in the 1st-round experiments. Therefore, in the discussion on the data of the 1st-
271 round experiments, we tried to minimize potential influences of the differences in the initial
272 TMB concentrations on the signals of HOMs by normalizing the HOMs signals with the initial
273 TMB signal. To precisely illustrate changes in the abundance of HOMs at different OH
274 exposures, a normalized signal was chosen to present the abundance of detected HOMs, which
275 is defined as the ratio of the signals of HOMs in the nitrate CIMS normalized by the reagent
276 ions and the initial signal of 1,3,5-TMB, i.e., $S(HOMs)/S(TMB)$. $S(HOMs)$ is the signal of
277 HOM detected by the nitrate CIMS normalized with the signal of reagent ions, whereas
278 $S(TMB)$ is the initial signal of 1,3,5-TMB detected by the Vocus PTR.

279 To compare chemical regimes of the two series of experiments and the ambient atmosphere,
 280 a PAM chemistry model (PAM_chem_v8), utilized widely in previous studies, were chosen
 281 with the latest updates to calculate radical profiles in our OFR (Li et al., 2015; Cheng et al.,
 282 2021; Wang et al., 2020b; Mehra et al., 2020; Lambe et al., 2015, 2018; Peng and Jimenez,
 283 2020; Lambe et al., 2017). This model is based on a photochemical box model that includes
 284 chemistry of photolysis of oxygen, water vapor, and other trace gases by the primary
 285 wavelengths of mercury lamps, and simplified VOC and RO₂ chemistry (Table S2), but further
 286 reactions of the first-generation stabilized products and the second-generation organic radicals
 287 are not considered. The reactions and corresponding kinetics utilized in this model were
 288 summarized in Table S2. In this work, autoxidation and accretion of 1,3,5-TMB-derived BPR,
 289 as well as subsequent reactions of the autoxidation product of BPR, i.e., C₉H₁₃O₇[•], are newly
 290 implemented or modified in this model (Reaction No. 46 – 62 in Table S2). These two radicals
 291 were the most significant RO₂ in the system and represented the whole RO₂ pool in the PAM
 292 chemistry model simulation. The pathways of peroxy radicals and their kinetics are discussed
 293 below. NO_x-related reactions are also included in the model. When experiments without NO_x
 294 are simulated, these NO_x-related reactions do not contribute to the simulation results.

295 The detailed reactions involved with RO₂ include:



306 R1, R2, and R3 are reactions of RO₂ + RO₂, forming alkoxy radicals, carbonyl termination
 307 products, and hydroxyl termination products, respectively. R4 is the accretion reaction,
 308 forming dimers via combination of two monomeric RO₂. R5 is the reaction between RO₂ and
 309 HO₂, forming hydroperoxyl radicals. The reaction rate constants for RO₂ in R1 – R5 are
 310 obtained by MCM or previous investigations (e.g., Jenkin et al., 2003; Berndt et al., 2018; Peng
 311 and Jimenez, 2020). We treat R1 – R3 as a total reaction with a reaction rate constant of 8.8×10⁻
 312 13 molecule⁻¹ cm³ s⁻¹, and branching ratios of R1 – R3 of 0.6, 0.2, and 0.2, respectively, as
 313 suggested by MCM (Jenkin et al., 2003). The reaction rate constants of BPR and C₉H₁₃O₇[•] for

314 $R4$ are 1.7×10^{-10} and 2.6×10^{-10} molecule⁻¹ cm³ s⁻¹, respectively (Berndt et al., 2018b). The
315 reaction rate constants for $R5$ is 1.5×10^{-11} molecule⁻¹ cm³ s⁻¹ (Jenkin et al., 2003).

316 $R6$ is the reaction between OH and RO₂, whose reaction rate constant is 1×10^{-10} molecule⁻¹
317 cm³ s⁻¹ according to previous studies (Bossolasco et al., 2014; Yan et al., 2016; Assaf et al.,
318 2016, 2017; Peng and Jimenez, 2020). Current knowledge on the reaction products for the
319 reaction of CH₃O₂· + OH, the most studied RO₂ + OH reaction, is summarized in Table S3. The
320 products of this reaction are suggested to include a Criegee intermediate (CH₂O₂·), a stabilized
321 methylhydrotrioxide (CH₃OOOH), an alkoxy radical (CH₃O·), and methanol (CH₃OH) (Yan et
322 al., 2016; Fittschen, 2019; Caravan et al., 2018; Müller et al., 2016). Müller et al. (2016) and
323 Caravan et al. (2018) suggested that the formation of CH₂O₂· is actually infeasible, and Yan et
324 al. (2016) estimated an upper limit branching ratio of 5% for this pathway. The branching ratios
325 of stabilized products CH₃OH and CH₃OOOH are 6 – 7% (Caravan et al., 2018; Müller et al.,
326 2016) and 7% (Müller et al., 2016), respectively. The most significant product of this reaction
327 is the alkoxy radical (CH₃O·), with a branching ratio of more than 86% (Müller et al., 2016).
328 In the absence of NO_x, CH₃OH and CH₃O· can also be formed via the traditional unimolecular
329 reaction between CH₃O₂· and RO₂, i.e., $R1$ and $R3$. The possible role of this reaction of large
330 RO₂, i.e., BPR and other C₉-RO₂, with OH has not yet been investigated. However, according
331 to the branching ratios for the reaction of CH₃O₂· + OH, this reaction is likely to form RO
332 instead of stabilized C₉ products. Hence, we assume that the branching ratios of hydrotrioxide
333 (ROOOH), RO, and ROH are 0.07, 0.86, and 0.07, respectively, for BPR + OH and C₉-RO₂ +
334 OH. reaction channels/products are proposed according to previous studies (Table S3).

335 $R7$ is the unimolecular reactions of RO₂ in the PAM OFR. RO₂ isomerization rate
336 coefficients are highly dependent on their structures, spanning from 10^{-3} – 10^6 s⁻¹ (Bianchi et
337 al., 2019; Crouse et al., 2013; Knap and Jørgensen, 2017; Praske et al., 2018). However, only
338 some substituted acyl RO₂ can undergo rapid isomerization at a reaction rate of 10^6 s⁻¹ (Knap
339 and Jørgensen, 2017). 1,3,5-TMB-derived BPR and its autoxidation product, C₉H₁₃O₇·, do not
340 belong to this group of substituted acyl RO₂ (Molteni et al., 2018; Tsiligiannis et al., 2019). The
341 most important unimolecular reactions for 1,3,5-TMB-derived BPR is likely autoxidation while
342 the precise autoxidation reaction rates of 1,3,5-TMB-derived BPR and other RO₂ in this system
343 are currently unclear (Bianchi et al., 2019; Molteni et al., 2018). Previous theoretical
344 investigations suggest that more than 90% BPR generated by the oxidation of 1,3,5-TMB
345 possess a structure favoring autoxidation and thus their overall autoxidation reaction rate is
346 relatively fast (Wang et al., 2017). We follow quantum calculation results on the autoxidation
347 reaction of a methyl group adjacent to the RO₂ functionality group (Wang et al. 2017), and time

348 the suggested rate (0.026 s⁻¹) by 3 due to the symmetry with three methyl groups in our parent
349 compound. The obtained autoxidation reaction rate is 0.078 s⁻¹.

350 ~~among which the autoxidation reaction rate is the most significant.~~ R8 and R9 are the
351 reactions between NO and RO₂, generating alkoxy radicals and organonitrates, respectively.
352 The reaction rate for the sum of these two reactions is 8.5×10⁻¹² molecule⁻¹ cm³ s⁻¹. The
353 branching ratios of these two reactions are 0.843 and 0.157, respectively, according to MCM
354 (Jenkin et al., 2003).

355 Alkoxy radicals, RO, will be generated in R1, R6, and R8. The widely used near-explicit
356 mechanism, MCM, assumes that RO formed via the alkoxy channel of BPR (R1) will
357 decompose into small molecules. Recently, Xu et al. (2020) probed the chemical fates of BPR-
358 derived RO, hereafter referred to as bicyclic alkoxy radical (BCP-oxy), in the oxidation of
359 benzene by laboratory experiments and model calculations, which can be taken as a reference
360 to induce the mechanism of 135-TMB-derived BCP-oxy. BCP-oxy can undergo two reactions,
361 i.e., ring-breakage and ring-closure, and a new calculation result suggests that the branching
362 ratio of ring-breakage reaction is larger than 98% (Wang et al., 2013). 56% of ring-breakage
363 reactions will break benzene-derived BCP-oxy into butenedial and glyoxal, and the rest 44%
364 will generate a C6 alkyl radical by a 1,5-aldehydic H-shift. The latter C6 alkyl radical will
365 further undergo other reactions, including a 93% branching ratio for decomposition reactions
366 that results in a reduction of carbon atom number (Xu et al., 2020). Therefore, most of benzene-
367 derived BCP-oxy will likely decompose into compounds with fewer carbon atoms. We assume
368 that 1,3,5-TMB-derived BCP-oxy will undertake these decomposition reactions with a similar
369 branching ratio, which means that these radicals cannot form a large number of stabilized
370 products that can influence the distributions of stabilized C9 products in nitrate CIMS.

371 R10 is the physical loss of RO₂. The physical loss of RO₂ in the PAM OFR consists of the
372 condensation loss to the aerosol particles and the diffusion loss to the OFR walls. In our
373 experiments, measurement results by a long-SMPS show that the aerosol particles presented in
374 the PAM OFR were few. The long SMPS consisted of a long-DMA (TSI model 3081) and a
375 CPC (TSI model 3787), covering a particle number size distribution from 13.6 nm to 736.5 nm.
376 Thus, though not detected in this study, we cannot absolutely deny the possibility that particles
377 might have been generated, resulting in a larger physical loss of HOMs. This part of physical
378 loss might be underestimated. The first-order loss rate of HOMs to the OFR walls, k_{wall} , is
379 limited by eddy diffusion and can be calculated with the following function (Cheng et al., 2021;
380 Palm et al., 2016; McMurry and Grosjean, 1985):

$$381 \quad k_{wall} = \frac{A}{V} \cdot \frac{2}{\pi} \cdot \sqrt{k_e D_g} \quad (Eq1)$$

where the OFR surface-area-volume ratio (A/V) is 25 m^{-1} and the coefficient of eddy diffusion (k_e) is 0.0042 s^{-1} , as estimated by the method utilized in a previous study (Brune, 2019) and given in Eq2.

$$k_e = 0.004 + 10^{-2.25} V^{0.74} \quad (\text{Eq2})$$

where V is the enclosure volume (m^3). The molecular diffusion coefficient, D_g , is estimated with the method as described by Fuller et al. (1966) and is around $5 \times 10^{-6} \text{ m}^2 \text{ s}^{-1}$ with 1,3,5-TMB derived BPR as an example. Hence, k_{wall} is around 0.0023 s^{-1} in the PAM OFR.

~~Other kinetic data~~ Kinetic data in the modified PAM_chem_v8 model are obtained from the IUPAC (International Union of Pure and Applied Chemistry) dataset (<https://iupac-aeris.ipsl.fr>, last access: 26 October 2023) and the MCM dataset (MCM v3.3.1, <https://mcm.york.ac.uk/MCM/>, last access: 9 October 2023), ~~except for those that are specifically discussed in details in the supplement. Note that the total RO_2 concentration is simplified to be the sum of concentrations of BPR and $\text{C}_9\text{H}_{13}\text{O}_7^+$. In this work, the autoxidation reaction and the accretion reaction of 1,3,5-TMB derived BPR, as well as the subsequent reactions of the autoxidation product of BPR, i.e., $\text{C}_9\text{H}_{13}\text{O}_7^+$, are newly implemented or modified in this model (Reaction No. 46–62 in Table S2). The newly implemented or modified reactions in this model are discussed in Supplementary Text S1. NO_x related reactions are also included in the model. When we simulate experiments without NO_x , these reactions do not contribute to the simulation results.~~

For the 1st-round experiments, the input parameters of temperature, mean residence time, water vapor concentration, O_3 concentration, and the initial 1,3,5-TMB concentration are $25 \text{ }^\circ\text{C}$, 53 s, 0.63%, ~~500–~~ $1.23 \times 10^{13} \text{ molecule cm}^{-3}$ ~~ppbv~~, and $1.23 \times 10^{12} \text{ molecule cm}^{-3}$ ~~50 ppbv~~, respectively, as measured directly. For the 2nd-round experiments, the input parameters of O_3 concentration and the initial 1,3,5-TMB concentration were updated as $3.68 \times 10^{12} \text{ molecule cm}^{-3}$ ~~150 ppbv~~ and $7.55 \times 10^{11} \text{ molecule cm}^{-3}$ ~~30.8 ppbv~~, respectively. In the NO_x experiments, the input flow rate of N_2O is 350 sccm in the 1st-round experiments and 2.5 slpm in the 2nd-round experiments, respectively. The actinic flux at 254 nm, I_{254} , is constrained by comparing OH exposures by model output and OH exposures estimated by the consumption of 1,3,5-TMB as measured by a the Vocus PTR. Consumption of O_3 estimated by the model agrees well with the measured results, with discrepancies being always within 10% at different OH exposures.

3 Results and discussion

3.1 Comparison of chemical regimes

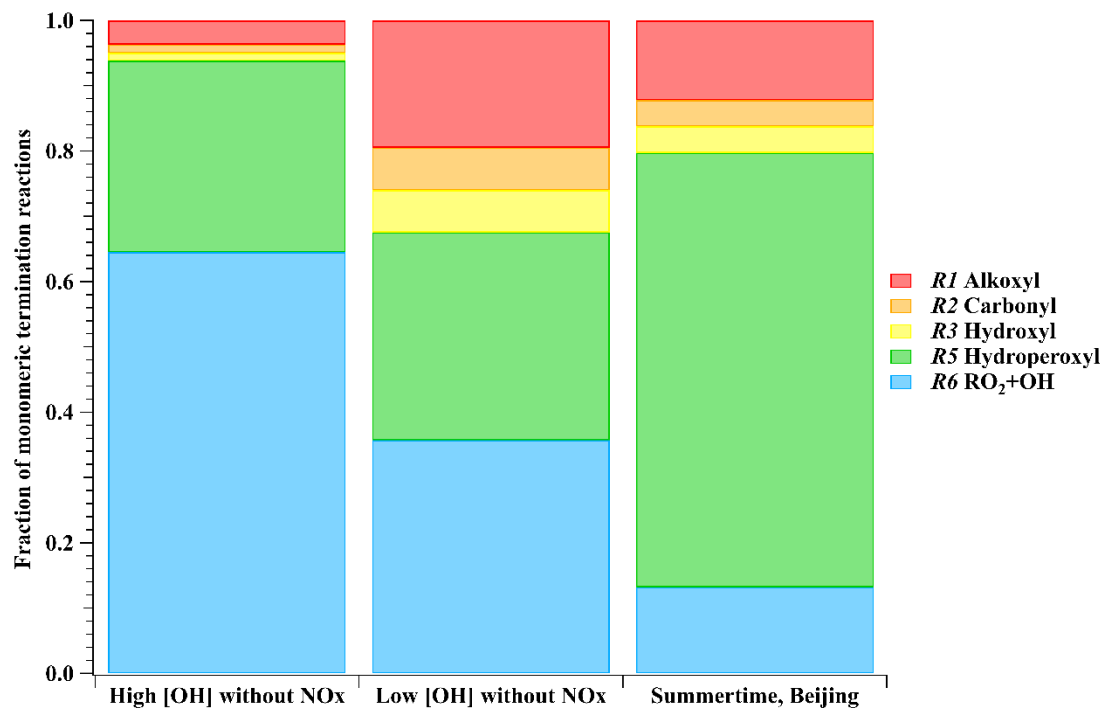
Concentration profiles of OH, RO_2 , and HO_2 as a function of OH exposures in our high [OH] experiments without NO_x , i.e., the 1st-round experiments, are illustrated in Figure S1a.

416 According to the modified PAM_chem_v8 model, when [OH] increased from 9.32×10^7 to
417 1.03×10^9 molecule cm^{-3} , [HO₂] increased from 7.25×10^8 to 2.79×10^9 molecule cm^{-3} , whereas
418 [RO₂] concentrations increased from 5.17×10^9 to 9.5×10^9 molecule cm^{-3} . The radical
419 concentrations in high [OH] experiments with NO_x (Figure S1b) varied in a similar range, with
420 [RO₂] ranging from 4.38×10^9 to 9.13×10^9 molecule cm^{-3} , HO₂ ranging from 4.47×10^9 to
421 6.47×10^9 molecule cm^{-3} , and OH ranging from 3.86×10^8 to 7.82×10^8 molecule cm^{-3} ,
422 respectively. The ratios of between HO₂/OH and RO₂/OH in the 1st-round experiments were
423 generally in the same order of magnitude as those in with the ambient atmosphere (Whalley et
424 al., 2021).

425 Radical concentrations were also estimated by the PAM_chem_v8 model to illustrate the
426 chemical regimes in the 2nd-round experiments (Table S4). The average [HO₂], [OH], and [RO₂]
427 were 9.7×10^7 , 1.64×10^7 , and 1.69×10^9 molecule cm^{-3} , respectively, in Exp. 2-3, and were
428 6.7×10^7 , 1.04×10^7 , and 1.34×10^9 molecule cm^{-3} , respectively, in Exp. 2-4, both of which
429 generally differ by no more than a factor of 3 from the summer daytime ambient ones in polluted
430 atmospheres (Tan et al., 2017, 2018, 2019; Whalley et al., 2021; Lu et al., 2012). The average
431 [HO₂], [OH], and [RO₂], as well as the NO and NO₂ concentrations in Exp. 2-7 are generally
432 very close to those in the same environment (Tan et al., 2019).

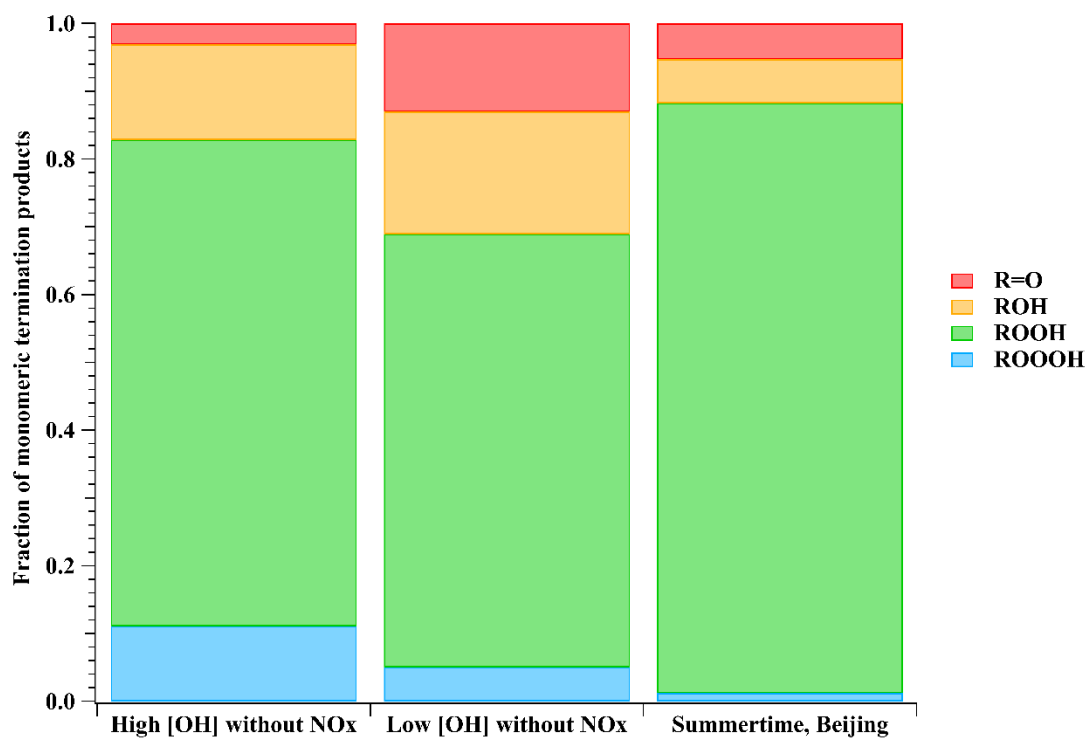
433 We take Exp. 1-12 ([OH] = $\sim 8.47 \times 10^8$ molecule cm^{-3} and NO_x = 0) and Exp. 2-3 ([OH] =
434 $\sim 1.64 \times 10^7$ molecule cm^{-3} and NO_x = 0) as representative examples and compare simulation
435 results with those from the ambient atmosphere, since NO_x in the ambient is believed not to
436 impact relative ratios for R1 – R3, R5, and R6. In the ambient atmosphere, the average [HO₂],
437 [OH], and [RO₂] were 2.7×10^8 , 8.0×10^6 , and 1.4×10^9 molecule cm^{-3} , respectively, around
438 summertime noon in urban Beijing (Whalley et al. 2021), and $(4 - 28) \times 10^8$, $(0.8 - 2.4) \times 10^7$,
439 and 1.2×10^9 molecule cm^{-3} (modeled) at a suburban site in Yangtze River Delta (Ma et al. 2022).
440 As shown in Figure 1a, for the most important RO₂, BPR, the fractions of monomeric
441 termination reactions of RO₂ + RO₂ (R1 – R3), RO₂ + HO₂ (R5), and RO₂ + OH (R6) were
442 6.2%, 29.3%, and 64.5%, respectively, in Exp.1-12. In contrast, the fractions were 32.5%,
443 31.8%, and 35.7%, respectively, in Exp. 2-3, whereas the values were 20.3%, 66.6%, and 13.2%,
444 respectively, for summertime, urban Beijing.

445 (a)



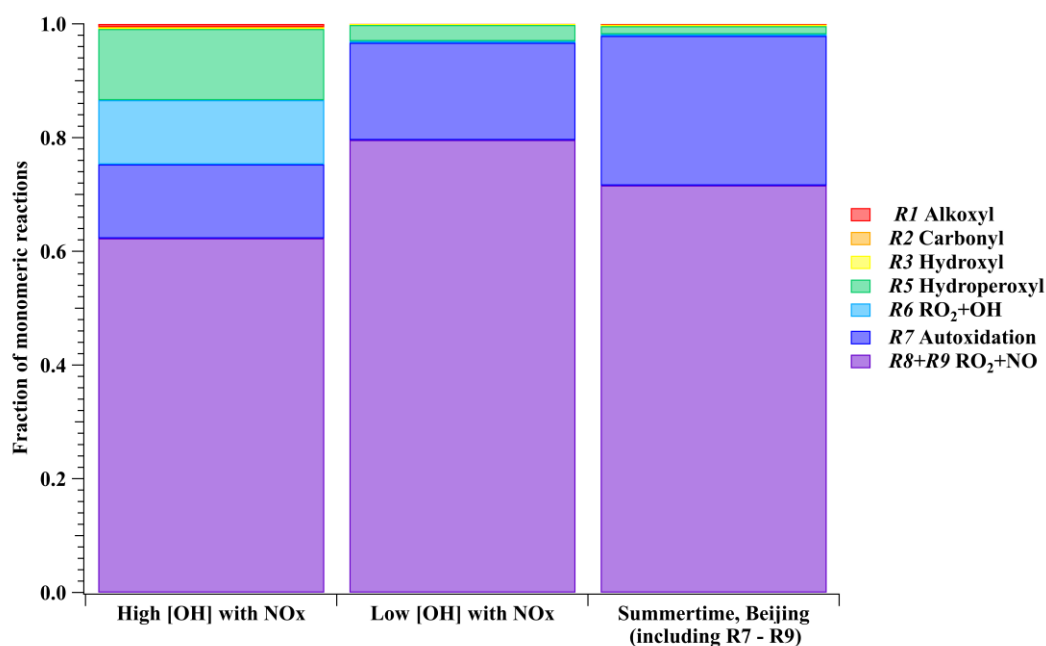
446

447 (b)



448

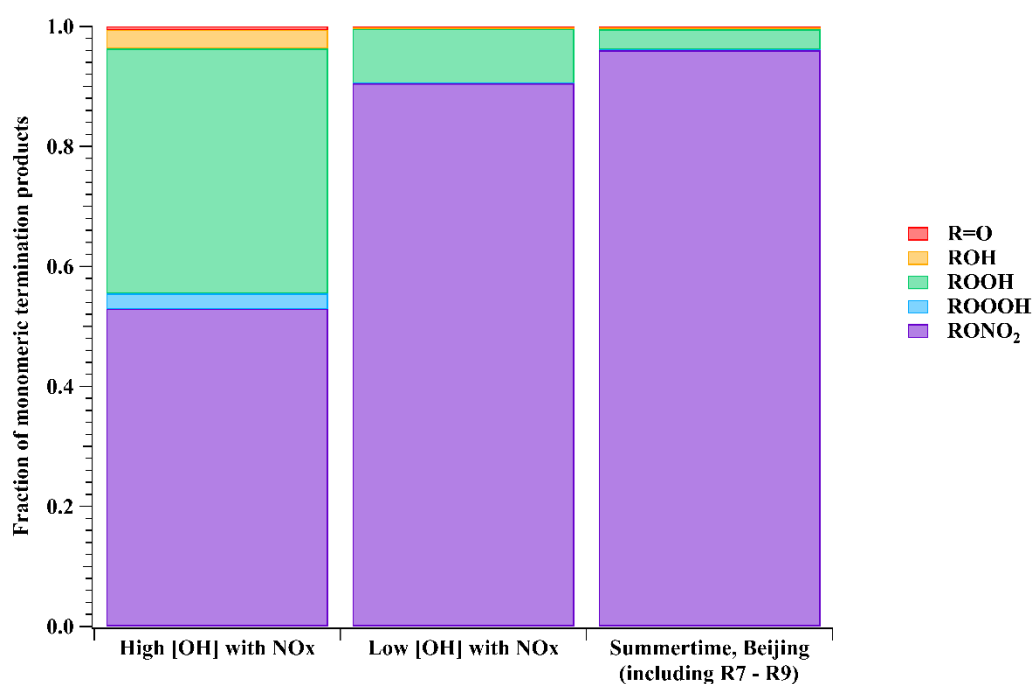
449 (c)



450

451

(d)



452

453 **Figure 1.** (a) The fraction of monomeric termination reactions and (b) monomeric termination
 454 products of BPR in a representative high [OH] experiment without NO_x (Exp. 1-12), a
 455 representative low [OH] experiment without NO_x (Exp. 2-3), and summertime, urban Beijing
 456 (Whalley et al. 2021). NO_x related reactions and products for the Beijing study are not included
 457 for a better comparison. (c) The fraction of monomeric reactions (R1 – R3 and R5 – R9) and
 458 (d) monomeric termination products of BPR in a representative high [OH] experiment with
 459 NO_x (Exp. 1-48), a representative low [OH] experiment with NO_x (Exp. 2-7), and summertime,

460 urban Beijing (Whalley et al. 2021). Reactions and kinetic rate coefficients used in the
461 calculations are provided in [Table S2](#).

462 ~~We take Exp. 1-12 ($[\text{OH}] = 8.47 \times 10^8 \text{ molecule cm}^{-3}$ and $\text{NO}_x = 0$) and Exp. 2-3 ($[\text{OH}] =$
463 $1.64 \times 10^7 \text{ molecule cm}^{-3}$ and $\text{NO}_x = 0$) as representative examples and compare simulation
464 results with those from the ambient atmosphere, since NO_x in the ambient is believed not to
465 impact relative ratios for $R1-R3$, $R5$, and $R6$. In the ambient atmosphere, the average $[\text{HO}_2]$,
466 $[\text{OH}]$, and $[\text{RO}_2]$ were 2.7×10^8 , 8.0×10^6 , and $1.4 \times 10^9 \text{ molecule cm}^{-3}$, respectively, around
467 summertime noon in urban Beijing (Whalley et al. 2021), and $(4-28) \times 10^8$, $(0.8-2.4) \times 10^7$, and
468 $1.2 \times 10^9 \text{ molecule cm}^{-3}$ (modeled) at a suburban site in Yangtze River Delta (Ma et al. 2022).
469 As shown in [Figure 1a](#), for the most important RO_2 , BPR, the fractions of monomeric
470 termination reactions of $\text{RO}_2 + \text{RO}_2$ ($R1-R3$), $\text{RO}_2 + \text{HO}_2$ ($R5$), and $\text{RO}_2 + \text{OH}$ ($R6$) were
471 6.2%, 29.3%, and 64.5%, respectively, in Exp. 1-12. In contrast, the fractions were 32.5%,
472 31.8%, and 35.7%, respectively, in Exp. 2-3, whereas the values were 20.3%, 66.6%, and 13.2%,
473 respectively, for summertime, urban Beijing.~~

474 Our NO_x -free experiments are characterized with an inherent drawback that the proportion
475 of the HO_2 termination pathway ($R5$) is actually lower than that under ambient conditions,
476 which is similar to most other laboratory experiments (Bianchi et al., 2019). In our high $[\text{OH}]$
477 experiments without NO_x , the reaction rates of unimolecular reactions, e.g., autoxidation
478 reaction ($R7$) and condensation ($R10$) did not change with $[\text{OH}]$ that increased in our
479 experiments relative to that in the ambient. As a result, relative proportions of autoxidation and
480 condensation ~~are were~~ lowered. On the other hand, 1,3,5-TMB-derived BPR was suggested to
481 undergo autoxidation ($R7$) at a reaction rate of 0.078 s^{-1} (Wang et al., 2017), which ~~represents~~
482 ~~represented~~ 36.8%, 94.4%, and 92.8% of the overall rates of $R1-R3$ and $R5-R7$ in Exp. 1-
483 12, Exp. 2-3, and summertime, urban Beijing, respectively. Because of its dominant proportion
484 in Exp. 2-3 and the ambient, the autoxidation channel is not included for clarity in [Figure 1a](#).
485 Autoxidation ~~does did~~ possess a lower significance in our high $[\text{OH}]$ experiments due to the
486 other accelerated bimolecular reactions. However, it would only influence the oxygen content
487 of our products but would not change the DBE. Both accretion reaction ($R4$) and condensation
488 ($R10$) have been taken into account in the model, but they would not influence the distributions
489 of monomeric stabilized products. We will specifically discuss these two pathways in the
490 following sections because of their complexity between the laboratory and ambient conditions.

491 RO_2 other than BPR and $\text{C}_9\text{H}_{13}\text{O}_7\cdot$ existed in the PAM OFR, which were not included in
492 the model simulation. Their reaction rates of the accretion reaction ($R4$) and the autoxidation
493 reaction ($R7$) should be different from BPR and $\text{C}_9\text{H}_{13}\text{O}_7\cdot$ due to the strong dependence of these
494 two reaction rates on the molecular structure. Rates for the other [reaction](#) channels, on the other

495 hand, should be the same as those of BPR and C₉H₁₃O₇. Therefore, their fates in terms of the
496 monomeric termination reactions (R1 – R3, R5 – R6, and R8 – R9) should be similar as
497 BPR and C₉H₁₃O₇.

498 Calculated from yields of stabilized monomeric termination products of BPR, the fractions
499 of monomeric termination reaction products in Exp. 1-12, Exp. 2-3, and summertime, urban
500 Beijing (Whalley et al. 2021) are presented in Figure 1b, showing a lot of similarities between
501 these conditions. The fractions of R=O, ROH, ROOH, and ROOOH in Exp. 1-12 were 3.1%,
502 14.1%, 71.7%, and 11.1%, respectively. These fractions were 13.0%, 18.1%, 63.9%, and 5.0%,
503 respectively, in the Exp. 2-3, ~~whereas the values and~~ were 5.3%, 6.5%, 87.0%, and 1.2%,
504 respectively, in the summertime Beijing case. Among them, the majority of products are always
505 ROOH and ROH, with ROOH being the most abundant. Therefore, the monomeric termination
506 products of BPR in our experiments are atmospheric relevant. In addition, only the R=O product
507 has a DBE higher than the reacted RO₂, but merely accounted for a limited proportion. All the
508 other stabilized termination products have a DBE that is 1 lower than the precursor, and are the
509 majority in both laboratory and ambient conditions. This indicates that the majority of the first-
510 generation products typically have a DBE that is 1 lower than that of 1,3,5-TMB, whereas the
511 majority of subsequent-generation products typically have a DBE that is 2 lower than that of
512 1,3,5-TMB. Once a monomeric compound with a DBE that is ≥at least 2 lower than that of
513 1,3,5-TMB was observed, multi-generation OH reactions have happened in the system.

514 In laboratory experiments in absence of NO_x (e.g., Exp.1-12), the proportions of R8 – R9 ,
515 i.e., the NO channel in the urban atmosphere were attributed to termination reactions of R1 –
516 R6, i.e., RO₂ + RO₂, accretion reaction, RO₂ + HO₂, and RO₂ + OH. By expanding proportions
517 of these termination reactions, laboratory investigations on product distributions can be
518 facilitated, as the detection of certain HOM products became more precise and the mass spectra
519 became simplified.

520 In experiments with NO_x, the chemical fates of BPR in high [OH] experiments (Exp. 1-48
521 as an example, [OH] = ~6.77×10⁸ molecule cm⁻³, NO = ~~~4.73×10¹⁰ molecule cm⁻³1.93 ppb~~,
522 NO₂ = ~~~1.67×10¹² molecule cm⁻³68 ppb~~), low [OH] experiments (Exp. 2-7 as an example, [OH]
523 = ~1.69×10⁷ molecule cm⁻³, NO = ~~~3.19×10¹⁰ molecule cm⁻³1.30 ppb~~. NO₂ = ~~~2.70×10¹¹~~
524 ~~molecule cm⁻³11 ppb~~), and the summertime, urban Beijing are compared. As shown in Figure
525 1c, in all three conditions, RO₂ reactions with NO were always the most significant pathway,
526 with autoxidation being the second most significant.

527 Accounting for at least 52% of monomeric termination products under all conditions,
528 organonitrates were always the most important termination products, as shown in Figure 1d.
529 On the other hand, based on the formulae of organonitrates, the detailed formulae ~~for of~~

530 monomer RO₂ could be probed, which can help us better understand the chemical reactions
531 inside the system. Alkoxy radicals generated in the NO termination channel will unlikely
532 influence the distributions of C₉ stabilized products since they tend to get decomposed in the
533 subsequent reactions, as discussed in [the Supplementary Text S1 our previous discussion on the](#)
534 [fate of alkoxy radicals in Section 2](#).

535 Due to the complexity of ambient RO₂ pool, it is difficult to estimate the detailed fraction
536 of accretion reactions R₄. In the laboratory experiments, RO₂ pool mainly consists of BPR and
537 its autoxidation reaction product C₉H₁₃O₇[•], which both can undergo accretion reaction rapidly
538 (Berndt et al., 2018b). The concentrations of these two radicals were estimated by
539 PAM_chem_v8 [according to the kinetics discussed in Supplementary Text S1](#). The reaction rate
540 of accretion (R₄) for BPR was around 1.61 s⁻¹ in Exp.1-12, being 88.4% of R₁ – R₇, and was
541 0.29 s⁻¹ in Exp.2-3, equivalent to 77.7% of R₁ – R₇. Certain uncertainties exist in the
542 estimation of the proportions of accretion reactions, as the PAM_chem_v8 model only includes
543 the first-generation reactions of precursors, whereas the subsequential fragmentation and re-
544 initiation of stabilized products can generate a series of new RO₂ that will influence the
545 proportions of accretion reactions. We are only certain that the significance of accretion
546 reactions in both Exp. 1-12 and Exp. 2-3 is larger than the ambient. The much-expanded
547 proportion of HOM dimers through accretion reactions makes it inadequate to compare yields
548 of HOM dimers and HOM monomers. However, this deviation will not influence our
549 conclusion on multi-generation OH oxidation and identification of HOM dimers can help us
550 identify the exact RO₂ in the OFR and confirm the conditions of secondary OH oxidation
551 according to the number of hydrogen atoms in the molecules.

552 In addition, certain compounds might have condensed onto pre-existing particles in the
553 real atmosphere before an appreciable fraction of such compounds undergoes the re-initiated
554 OH oxidation. Therefore, even [if](#) the same product can be generated both in the laboratory
555 experiments and the ambient atmosphere, the relative significance of this product is not
556 completely identical. Though OOMs might have the potential to undergo multi-generation OH
557 oxidation, the exact proportion of this reaction in the ambient strongly depends on their
558 volatility, in other words, condensation sink of these OOMs. The typical monomeric
559 termination products of 1,3,5-TMB-derived BPR, C₉H₁₂O₄, C₉H₁₄O₄, C₉H₁₄O₅, and C₉H₁₃NO₆,
560 are estimated to have saturation vapor concentrations (C*) of 30.20, 30.20, 0.85, and 3.39 μg/m³
561 at 300 K, [respectively](#) with the volatility parameterization developed in the CLOUD chamber
562 oxidation experiments of aromatics, [respectively](#) (Wang et al., 2020a). From the perspective of
563 volatility, they all belong to semi-volatile organic compounds (SVOC, 0.3 < C* < 300 μg/m³)
564 and are expected to exist in both the condensed and the gas phases at equilibrium in the

565 atmosphere (Bianchi et al., 2019). Compared to ambient conditions, the proportion of their
566 condensation ~~rates~~ in the laboratory were biased to be lower due to the accelerated bimolecular
567 reactions. However, this will not prevent the high [OH] experiments from showing the potential
568 and ability of these compounds to go through re-initiated OH oxidation, as these compounds
569 would exist in significant fractions in the gas phase in the real atmosphere.

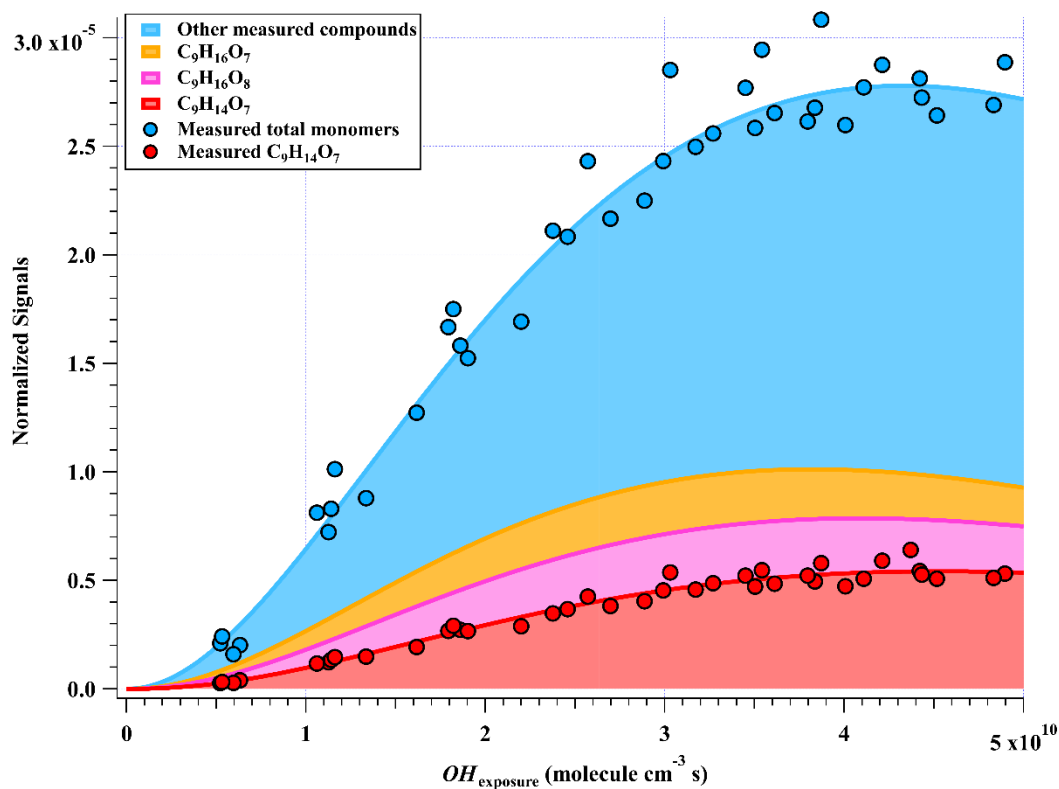
570 However, the conditions are completely ~~distinct~~ different for other HOM monomer
571 products and HOM dimer products with much lower volatility. It is difficult for a HOM dimer,
572 e.g., C₁₈H₂₆O₁₀ estimated with a C* of 7.24×10⁻¹³ μg/m³ at 300 K, to survive long enough to
573 experience an appreciable re-initiated photochemical ageing. The lifetime of HOMs that can be
574 classified as LVOCs (3×10⁻⁵ < C* < 0.3 μg/m³) and ELVOCs (C* < 3×10⁻⁵ μg/m³) can be
575 estimated according to the condensation sink (CS) in the atmosphere, as they are lost
576 irreversibly onto surfaces. The median value of CS in urban Beijing was reported to be around
577 0.019 s⁻¹ and 0.057 s⁻¹ during NPF days and non-NPF days, respectively, whereas the values in
578 Shanghai were reported to be around 0.013 s⁻¹ and 0.017 s⁻¹. respectively (Deng et al., 2020;
579 Yao et al., 2018), which are all much higher than the physical loss in our PAM OFR, i.e., 0.0023
580 s⁻¹, ~~as stated in the~~ Supplementary Text S1. LVOCs and ELVOCs are believed to be lost
581 irreversibly to the surface in both the laboratory and ambient because of their low volatility.
582 ~~However, b~~By assuming a similar diffusion coefficient of LVOCs and ELVOCs to that of
583 sulfuric acid, the lifetimes of LVOCs and ELVOCs in the ambient still can still be as high as 77
584 s for the condensation loss, which is close to the residence time of our PAM OFR. Therefore, if
585 ~~LVOCs and ELVOCs they were generated by oxidation of aromatics in the ambient, these~~
586 ~~LVOCs and ELVOCs~~ should at least have the potential to experience the same OH exposures
587 ~~in the ambient~~ as those in our low [OH] experiments, i.e., at least 5.86×10⁸ molecule cm⁻³ s, ~~if~~
588 ~~they were generated~~. On the other hand, the detailed proportions of LVOCs and ELVOCs after
589 a large OH exposure should be lower than those in the lab due to their magnified physical loss
590 in the ambient. This means that if the multi-generation products of those compounds were
591 observed in the ambient air, they should have been generated via a reaction that happened very
592 recently.

593 3.2 Oxidation products in high [OH] experiments

594 A total of 33 HOM monomers with formulae of C₇₋₉H₈₋₁₆O₆₋₁₁ and 22 HOM dimers with
595 formulae of C₁₇₋₁₈H₂₄₋₃₀O₈₋₁₄ were observed in the 1st-round experiments of gas phase OH-
596 initiated oxidation of 1,3,5-TMB in the OFR, i.e., high [OH] experiments, as listed in Table S5.
597 The relative signal contributions of HOMs to the total signals of all HOMs at an OH exposure
598 of 2.38×10¹⁰ molecules cm⁻³ s are listed as an example in Table S5. The most abundant HOM
599 products were also shown in stack in Figure 2, whose relationships with OH exposures are

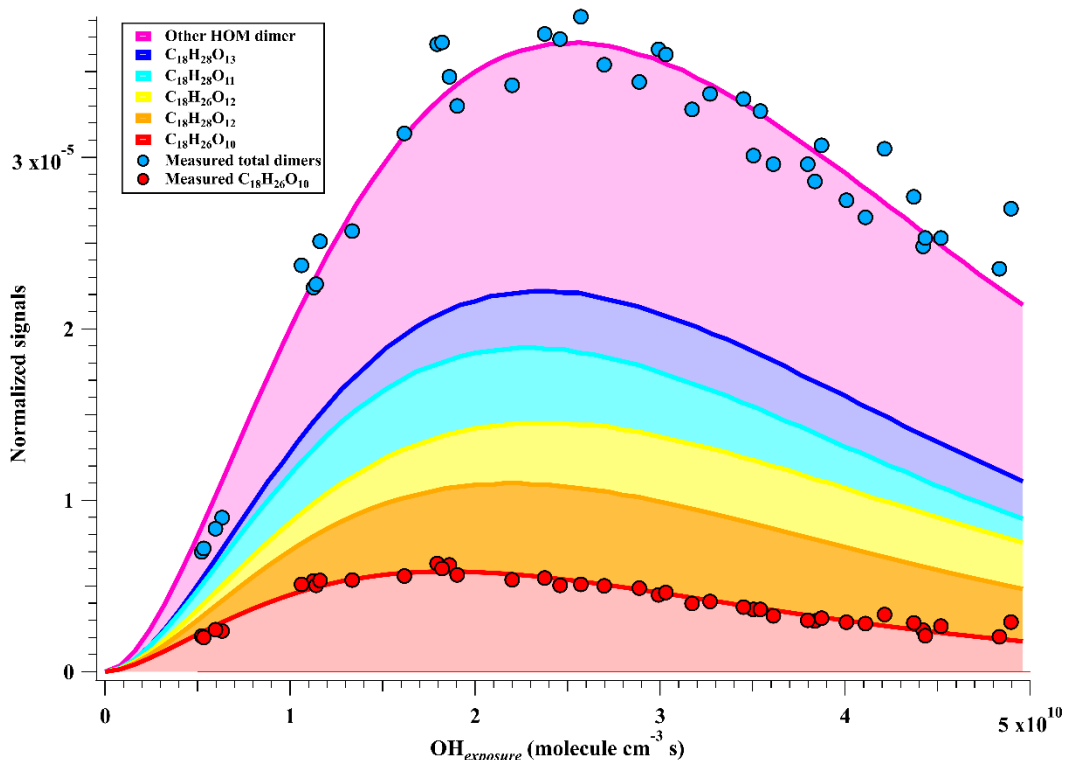
600 superimposed by a gamma function ($f(x) = ax^m e^{-x}$) simulation line to guide the eyes. The
 601 sum of normalized HOM monomers' abundance increased monotonically up to the highest OH
 602 exposure of 5×10^{10} molecule cm^{-3} s, whereas those of HOM dimers showed a non-monotonic
 603 dependence on OH exposure. The observed faster increase of accretion products than that of
 604 HOM monomers can be explained jointly by the fast second-order kinetics for accretion
 605 reactions of RO_2 (Berndt et al., 2018b) and the high concentrations of relevant radicals in this
 606 work. On the other hand, most of the first-generation HOM dimers formed from accretion
 607 reactions contain at least one C=C bond and have more functionalities than HOM monomers,
 608 and thus should be more reactive to OH radicals, which, together with a faster deposition loss
 609 of dimers, results in a faster consumption of HOM dimers than monomers in the OFR. The
 610 faster production and consumption of HOM dimers allowed their concentrations to summit at
 611 middle levels of OH exposures. As stated in Section 3.1, because of the inherent disadvantage
 612 of laboratory experiments, $[\text{RO}_2]$ is always too high in the OFR, which has been pointed out in
 613 a previous study (Bianchi et al., 2019). The accretion reactions in the OFR are relatively more
 614 significant than it should be in the ambient atmosphere. We do not mean to compare the
 615 abundance of HOM monomer and HOM dimer signals crossly here, but to pay attention to the
 616 if formulae molecular characterization.

617 (a)



618

619 (b)



620

621 **Figure 2.** Normalized signals of (a) HOM monomers and (b) HOM dimers versus OH exposure
 622 in the high [OH] experiments, which are fitted via a gamma function and shown in stack.

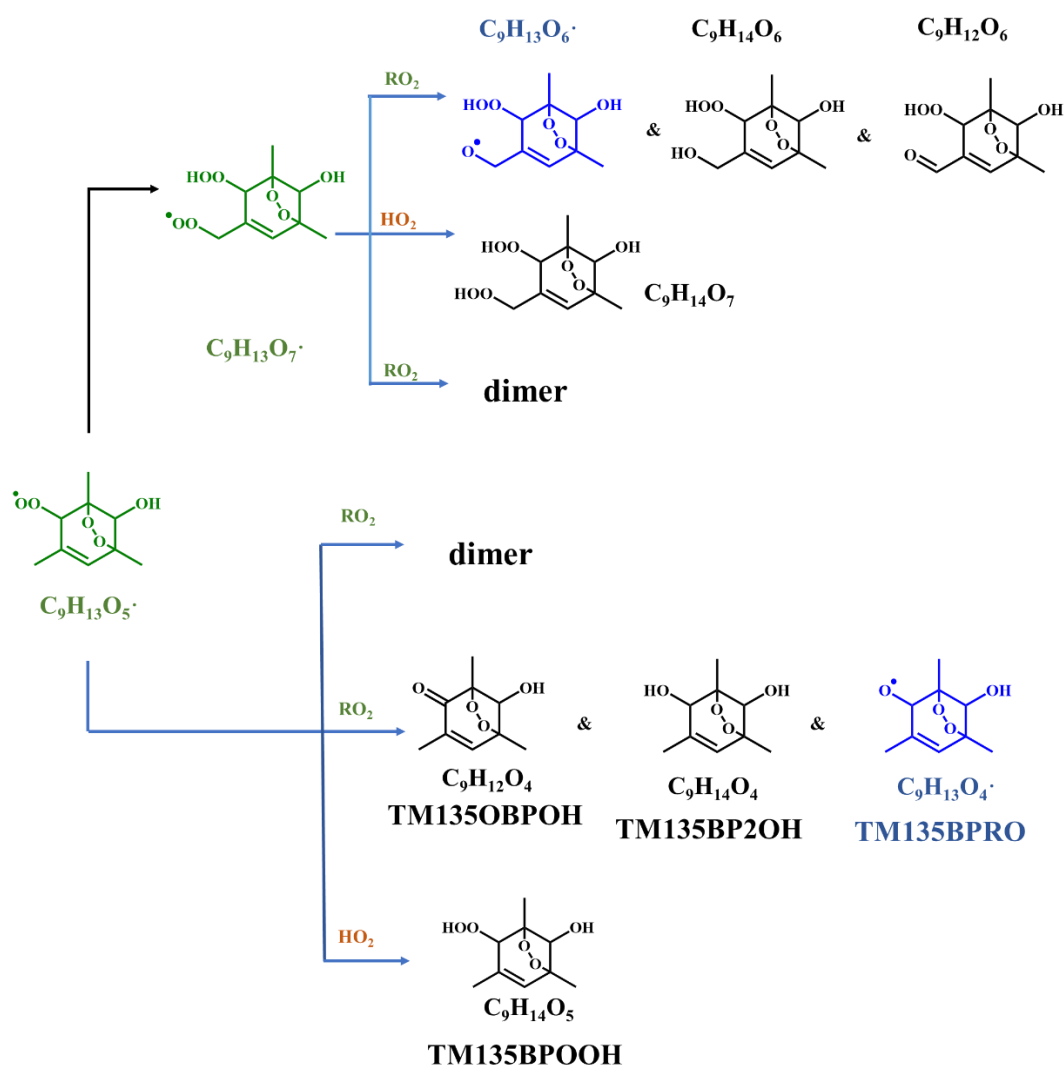
623

Theoretically, at a given RH and UV (i.e., a given [OH]), an increase in the initial TMB
 624 would lead to formation of more RO₂, which corresponds to a larger RO₂/OH. However, under
 625 our high [OH] experimental conditions, the RO₂/OH/HO₂ channels of RO₂ radicals are always
 626 minor, and thus an increase in RO₂/OH would not have a significant impact on the relative
 627 distribution of products formed from these channels. We compared product MS for experiments
 628 with a similar OH exposure but different initial concentrations of TMB (e.g., Exp. 1-3 v.s. Exp.
 629 1-19, and Exp. 1-12 v.s. Exp. 1-22). The OH exposures of Exp. 1-3 and Exp. 1-19 were
 630 estimated by the consumption of precursors to be 5.2×10^9 and 5.3×10^9 molecule cm⁻³ s,
 631 respectively, but the initial concentration of TMB of Exp. 1-3 was 25% more than that in Exp.
 632 1-19. Meanwhile, the OH exposures of Exp. 1-12 and Exp. 1-22 were 4.5×10^{10} and 4.4×10^{10}
 633 molecule cm⁻³ s, respectively, but the initial concentration of TMB of Exp. 1-12 was 48% more
 634 than that in Exp. 1-22. [Figure S2 shows c](#)Comparisons between the product MS of Exp. 1-3
 635 and Exp. 1-19 ([Figure S2](#)), as well as of Exp. 1-12 and Exp. 1-22, [show-indicating](#) that increase
 636 in the initial concentration of precursors generally resulted in a minor increment in the absolute
 637 signals of HOMs. Clearly, the relative distributions of products in these experiments are quite
 638 similar, indicating a minor difference in the relative distributions of products caused by
 639 fluctuations of initial concentrations of TMB.

640

3.2.1 HOM monomers

641 Previous studies indicate that oxidation products derived from the peroxide-bicyclic
642 pathway represent a main fraction of HOMs (Wang et al., 2017; Zaytsev et al., 2019). For 1,3,5-
643 TMB, this pathway, as recommended by ~~Master Chemical Mechanism (MCM)~~, starts from a
644 BPR, $C_9H_{13}O_5^\bullet$ (MCM name: TM135BPRO2) (Molteni et al., 2018). According to MCM and
645 Molteni et al. (2018), Scheme 1 has been proposed to provide a good understanding of this
646 reaction system and the structures of oxidation products. Molteni et al. (2018) suggested that
647 $C_9H_{13}O_7^\bullet$, i.e., peroxy radical formed from autooxidation of $C_9H_{13}O_5^\bullet$ has two isomers. A
648 second-step of endo-cyclization is required in the formation of one of the isomer, which is
649 extremely slow and not competitive as shown in several previous studies using both
650 experimental and theoretical approaches (Wang et al., 2017; Xu et al., 2020). Even if such a
651 second O_2 bridging to a double bond is assumed to be possible, the abundance of this isomer
652 should be significantly smaller than the other one, because of the much faster reaction rate of
653 H-shift reaction. Therefore, we do not take the $C_9H_{13}O_7^\bullet$ isomer containing a double endo-
654 cyclization into consideration in this work. The majority of HOM monomers is generated from
655 subsequent reactions of $C_9H_{13}O_5^\bullet$ and newly formed $C_9H_{13}O_7^\bullet$, both of which contain one C=C
656 bond in the carbon backbone and thus have a feasible site for OH addition. Meanwhile, the
657 autooxidation reaction rate for newly formed $C_9H_{13}O_7^\bullet$ should be significantly smaller than
658 $C_9H_{13}O_5^\bullet$, as there is no hydrogen atom in $C_9H_{13}O_7^\bullet$ that is able to undergo a hydrogen atom
659 shift at an appreciable rate based on our current understanding. Therefore, the subsequent
660 autooxidation reaction should not be able to generate large amounts of more oxidized RO_2 .

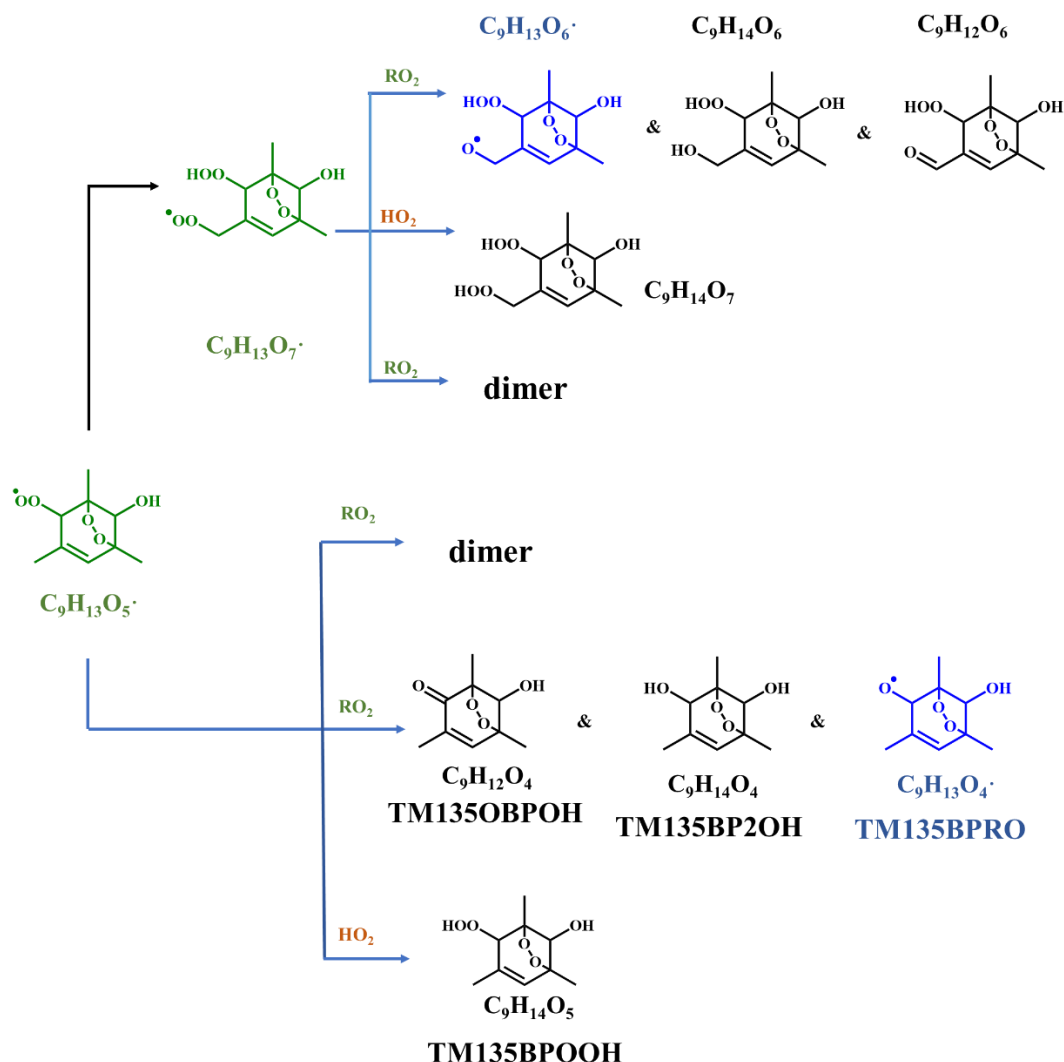


661

662 ~~Scheme 1. Oxidation pathways of the bicyclic peroxy radical $C_9H_{13}O_5\cdot$ (MCM name:~~
 663 ~~TM135BPRO2) in the OH-initiated oxidation of 1,3,5-TMB. Green, blue, and black formulae~~
 664 ~~denote alkyl peroxy radicals, alkoxy radicals and stabilized products, respectively. Black~~
 665 ~~arrows denote the autoxidation pathway. MCM names for HO_2 - and RO_2 -termination products~~
 666 ~~of TM135BPRO2 are present.~~

667 Monomeric termination products of BPR, as shown in **Scheme 1**, were not detected by
 668 nitrate CIMS in this round of experiments, which might be due to the fast sub-sequential OH
 669 oxidation of these products under high [OH] environment since they were observed under low
 670 [OH] environments as shown in Section 3.3. Monomeric termination products of $C_9H_{13}O_7\cdot$ were
 671 all observed clearly, including $C_9H_{12}O_6$, $C_9H_{14}O_6$, and $C_9H_{14}O_7$. Especially, $C_9H_{14}O_7$ was the
 672 most abundant one among all of the HOM monomer products (**Figure 2a**). As proved by a
 673 previous study, these three species should be typical first-generation stabilized products derived
 674 from autoxidation (Wang et al., 2020b). These HOM monomers should consist of several

675 isomers bearing the same formula, because products from the secondary reactions cannot share
 676 the same structure as that of the one from the first-generation reaction. However, limited by the
 677 inherent disadvantages of mass spectrometers, we could not distinguish isomers here and
 678 further illustrate their different chemical behaviors.



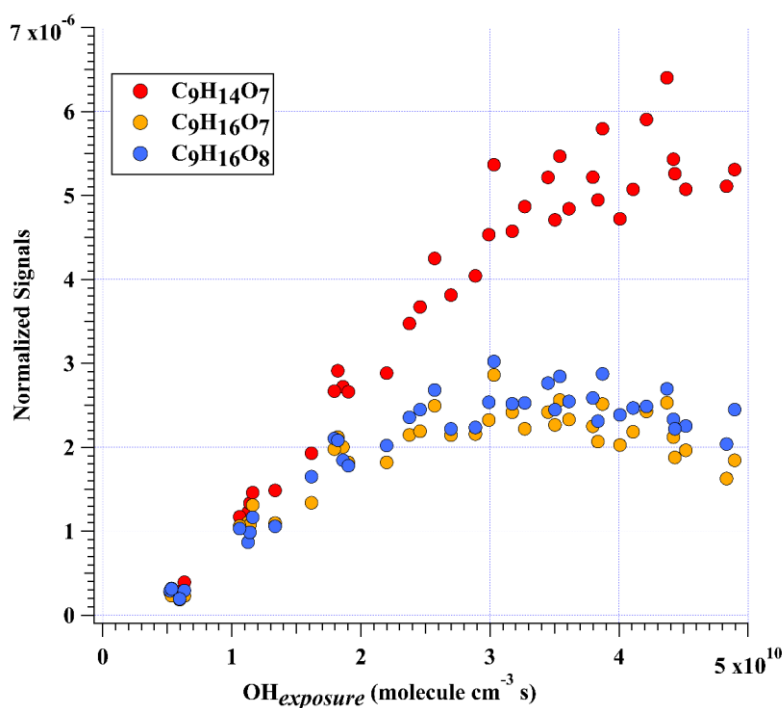
679

680 **Scheme 1.** Oxidation pathways of the bicyclic peroxy radical $C_9H_{13}O_5\cdot$ (MCM name:
 681 TM135BPRO2) in the OH-initiated oxidation of 1,3,5-TMB. Green, blue, and black formulae
 682 denote alkyl peroxy radicals, alkoxy radicals and stabilized products, respectively. Black
 683 arrows denote the autoxidation pathway. MCM names for HO_2 - and RO_2 -termination products
 684 of TM135BPRO2 are present.

685 In addition to these three ones, the next most prominent products to $C_9H_{14}O_7$ were $C_9H_{16}O_7$
 686 and $C_9H_{16}O_8$ (Figure 3a), which are produced from multi-generation oxidation according to
 687 their DBE. Based on the formulae of these three HOM monomers, they ($C_9H_{14}O_7$, $C_9H_{16}O_7$, and
 688 $C_9H_{16}O_8$) could be formed from the bimolecular termination reactions of $C_9H_{15}O_8\cdot$, which can

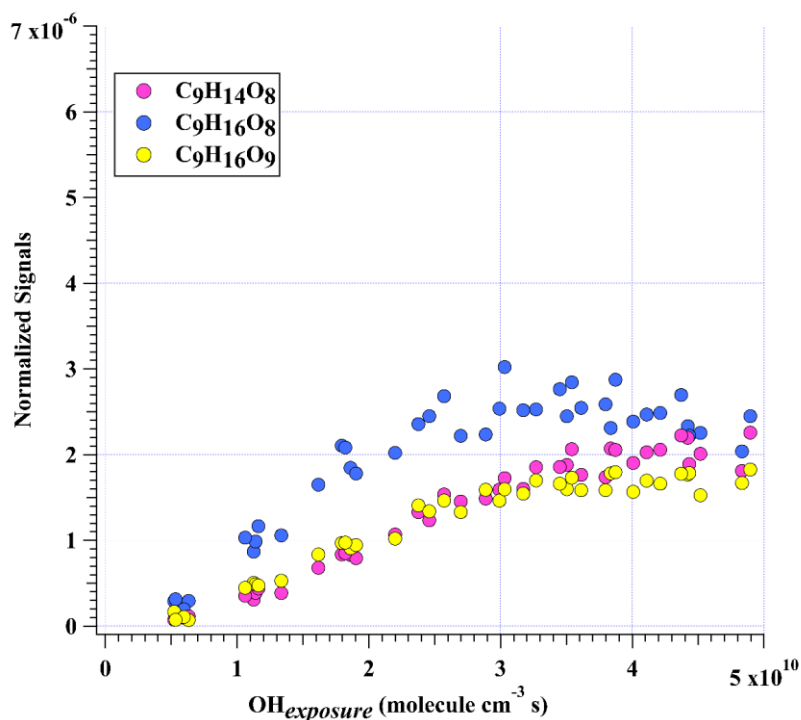
689 be generated by an OH attack to $C_9H_{14}O_5$ (Scheme 2), the hydroperoxyl termination product of
690 the BPR, $C_9H_{13}O_5^\bullet$. The other HOM monomers characterized with high signals were $C_9H_{14}O_8$
691 and $C_9H_{16}O_9$ (Figure 3b). These two HOM monomers ($C_9H_{14}O_8$ and $C_9H_{16}O_9$), together with
692 $C_9H_{16}O_8$, correspond to the monomeric termination products of $C_9H_{15}O_9^\bullet$, which is highly likely
693 the peroxy radical generated by an OH attack to $C_9H_{14}O_6$ (Scheme 3), i.e., the hydroxyl
694 termination product of $C_9H_{13}O_7^\bullet$. As discussed earlier, $C_9H_{13}O_7^\bullet$ is a typical autoxidation
695 reaction product of the BPR of $C_9H_{13}O_5^\bullet$. Therefore, detected signals of $C_9H_{16}O_8$ should be the
696 sum of two isomers' signals at least. Other HOM monomers were generally observed at much
697 lower signals and thus were not plotted individually.

698 (a)



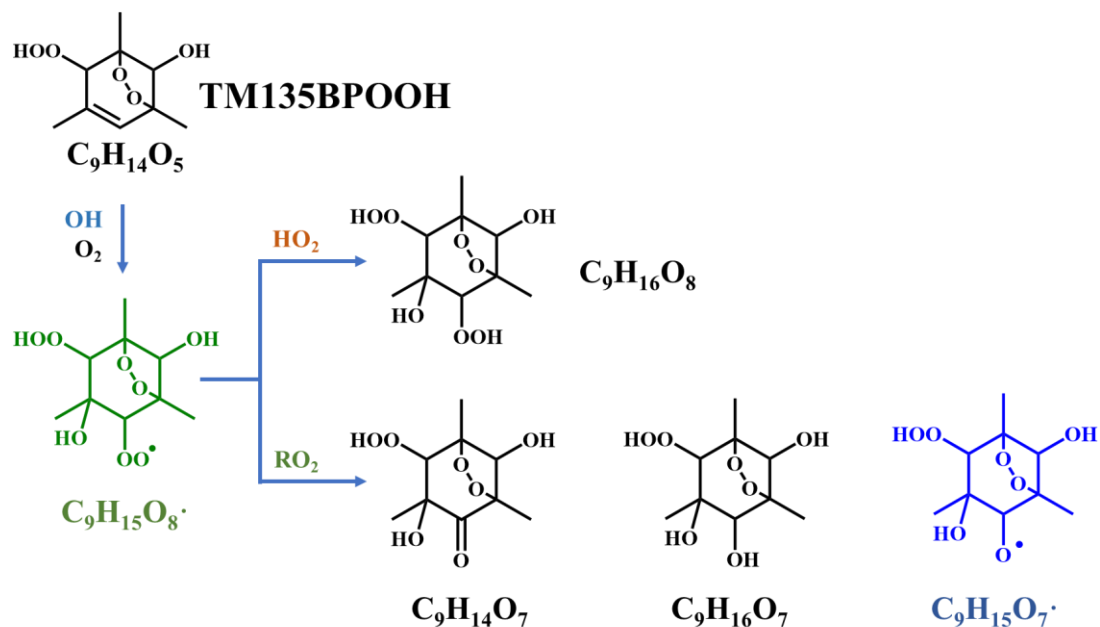
699

700 (b)



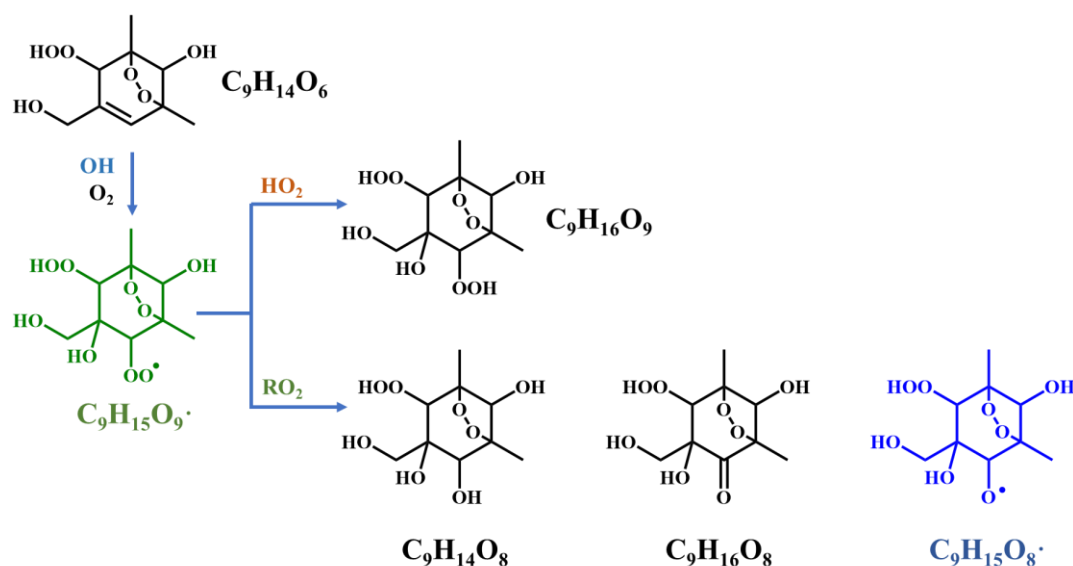
701

702 **Figure 3.** Normalized signals of (a) C₉H₁₄O₇, C₉H₁₆O₇, and C₉H₁₆O₈ and (b) C₉H₁₄O₈, C₉H₁₆O₈,
 703 and C₉H₁₆O₉ measured at the exit of OFR in our high [OH] experiments without NO_x as a
 704 function of OH exposure. C₉H₁₆O₈ are shown in both plots to better illustrate the chemical
 705 profiles of different compound groups.



706

707 **Scheme 2.** Proposed formation pathways of C₉H₁₄O₇, C₉H₁₆O₇, and C₉H₁₆O₈ via the secondary
 708 OH oxidation of TM135BPOOH.

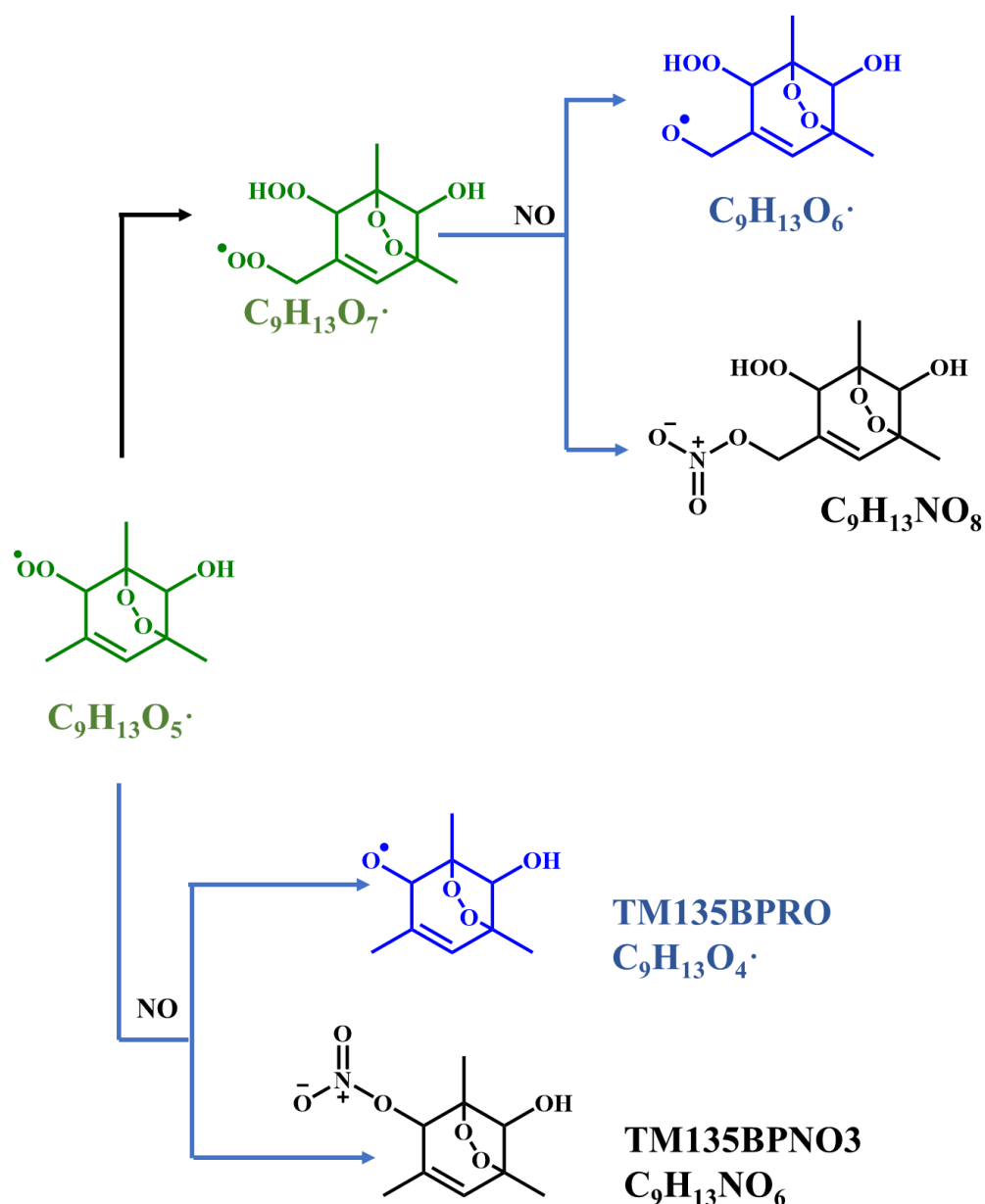


709

710 **Scheme 3.** Proposed formation pathways of C₉H₁₄O₈, C₉H₁₆O₈, and C₉H₁₆O₉ via the secondary
 711 OH oxidation of TM135BPOOH.

712 It is worth noting that HOM monomers with 18 hydrogen atoms, i.e., a DBE of 1, were
 713 never observed in our experiments, including a potential stabilized hydroperoxyl products
 714 formed from C₉H₁₇O_m·. This is expected, since C₉H₁₇O_m· should be in really low concentrations,
 715 if ever existed. As indicated by its hydrogen number, a C₉H₁₇O_m· was formed by at least two
 716 OH additions to the C=C bond of a C₉H₁₃O_m·, but the main BPR, C₉H₁₃O₅·, and its autoxidation
 717 product (C₉H₁₃O₇·), are characterized with one C=C bond on the ring, which makes this
 718 formation pathway impossible. Other ring-breakage pathways should not contribute to the
 719 formation of this radical (C₉H₁₇O_m·) because of their low branching ratio as determined by
 720 recent studies (Zaytsev et al., 2019; Xu et al., 2020).

721 Proposed according to MCM and Molteni et al. (2018), **scheme 4** shows the NO
 722 termination pathways of the main BPR C₉H₁₃O₅· and its autoxidation product, C₉H₁₃O₇·. After
 723 introducing N₂O into PAM OFR, quantities of organonitrates were generated, including both
 724 C9 and C18 organonitrates. The averaged mass spectrometry of nitrate CIMS in the 4.41×10^{10}
 725 molecule cm^{-3} ~~1.8 ppb~~ NO experiment and 1.18×10^{11} molecule cm^{-3} ~~4.8 ppb~~ NO experiment is
 726 shown in **Figure S3**. Organonitrates were formed via the NO + RO₂ reaction, called as NO
 727 termination reactions. The distribution of oxidation products under these two NO settings were
 728 similar.



729

730 **Scheme 4.** NO termination reactions of the bicyclic peroxy radical $C_9H_{13}O_5\cdot$ (MCM name:
 731 TM135BPRO2) and its autoxidation reaction products. Green, blue, and black formulae denote
 732 alkyl peroxy radicals, alkoxy radicals and stabilized products, respectively. Black arrows
 733 denote the autoxidation pathway. MCM names of NO-termination products of TM135BPRO2
 734 are present.

735 As discussed above, most of the first-generation HOMs should contain a C=C bond in the
 736 carbon backbone. The ubiquitous existence of organonitrates that contain two nitrogen atoms
 737 exactly confirms the extensive secondary OH oxidation in the systems, because the NO
 738 termination reaction of RO_2 is the only pathway that can generate organonitrates in our
 739 experiments and this pathway can only introduce one nitrogen atom at a time, as indicated in
 740 **Scheme 4**. RO_2 can react with NO_2 to form peroxy nitrates ($ROONO_2$) but these species are

741 thermally unstable except at very low temperatures or when the RO₂ is an acylperoxy radical
742 (Orlando and Tyndall, 2012), neither of which were not met in our experiments. The
743 concentrations of NO₃ were estimated to be lower than ~~1-2.45×10⁷ molecule cm⁻³ pptv~~ by our
744 modified PAM_chem_v8 because of the existence of decent concentrations of NO, which
745 would consume NO₃ at a rapid reaction rate, i.e., 2.7×10⁻¹¹ molecule⁻¹ cm³ s⁻¹ (IUPAC dataset ,
746 <https://iupac-aeris.ipsl.fr>, last access: 26 October 2023). Therefore, NO₂ and NO₃ were not
747 likely to react with RO₂ to form large amounts of organonitrates in our experiments. Taking the
748 most abundant organonitrate, C₉H₁₄N₂O₁₀, as an example, it was exactly the NO termination
749 product of C₉H₁₄NO₉•, which was generated from an OH attack and a subsequent O₂ addition
750 to C₉H₁₃NO₆, the NO termination product of C₉H₁₃O₅•. For other organonitrates, C₉H₁₃NO₈, the
751 second most abundant organonitrate, could be either a NO termination product of C₉H₁₃O₇• or,
752 together with other most abundant organonitrates, C₉H₁₅NO₇ and C₉H₁₅NO₈, classical
753 termination products of C₉H₁₄NO₉•. C₉H₁₄N₂O₁₀, C₉H₁₅NO₇, and C₉H₁₅NO₈ all have a DBE of
754 2 lower than the precursor and thus are the typical multi-generation OH oxidation products.

755 The NO:RO₂ ratio in the PAM OFR in this series of experiments is lower than typical
756 values in the ambient atmosphere, which is due to the existence of O₃ that was utilized to
757 generate O(¹D) in the OFR and its rapid reaction rate with NO. However, due to rapid reaction
758 rate constants between NO and RO₂, i.e., around 8.5×10⁻¹² molecule⁻¹ cm³ s⁻¹, the reaction rate
759 for the NO termination channel of RO₂ was as fast as around 0.3 – 1.0 s⁻¹. Large amounts of
760 organonitrates would still be formed, as discussed in Section 3.1. Our conclusion is also valid
761 because of detection of compounds with multiple nitrogen atoms.

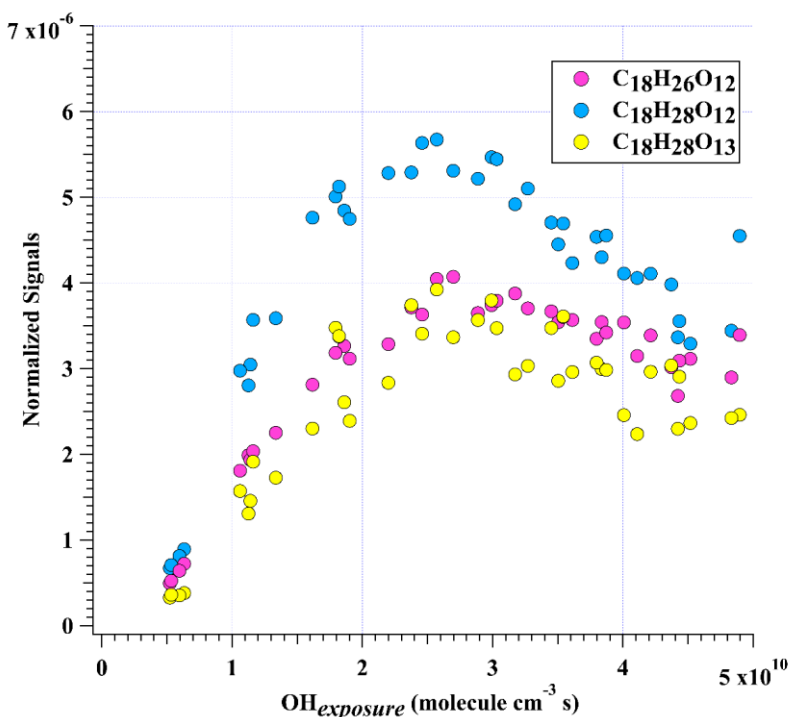
762 3.2.2 HOM dimers

763 Accretion reaction RO₂ + RO'₂ → ROOR' + O₂ is a source of gas-phase dimer
764 compounds from highly oxidized, functional RO₂ radicals (Ehn et al., 2014; Berndt et al., 2018b;
765 Zhao et al., 2018; Berndt et al., 2018a). C₁₈H₂₆O₈ and C₁₈H₂₆O₁₀ are two typical accretion
766 reaction products in the 1,3,5-TMB + OH system, whose formation pathways have been
767 elucidated (Berndt et al., 2018b). C₁₈H₂₆O₈ can only be formed via the accretion reaction of two
768 C₉H₁₃O₅•. C₉H₁₃O₃• is not likely to react with C₉H₁₃O₇• to form large amounts of C₁₈H₂₆O₈.
769 C₉H₁₃O₃• can only be formed after addition of a hydroxyl radical to the aromatic ring of 1,3,5-
770 TMB and a subsequent O₂ addition to the newly formed hydroxyl-substituted cyclohexadienyl
771 radical (Vereecken, 2019). However, the lifetime of this radical is extremely short, as C₉H₁₃O₃•
772 will undertake a ring-closure reaction and get attached by a O₂ very rapidly, forming BPR,
773 C₉H₁₃O₅•. Its short lifetime and low concentration, as indicated by Berndt et al. (2018), lead to
774 its insignificant role in the accretion reactions. In contrast, C₁₈H₂₆O₁₀ can be formed either by
775 the accretion reaction between C₉H₁₃O₅• and C₉H₁₃O₇• or via a second OH attack to C₁₈H₂₆O₈.

776 These two HOM dimers are so far the only ones that are confirmed to be formed via the
777 accretion reactions (Berndt et al., 2018b; Bianchi et al., 2019).

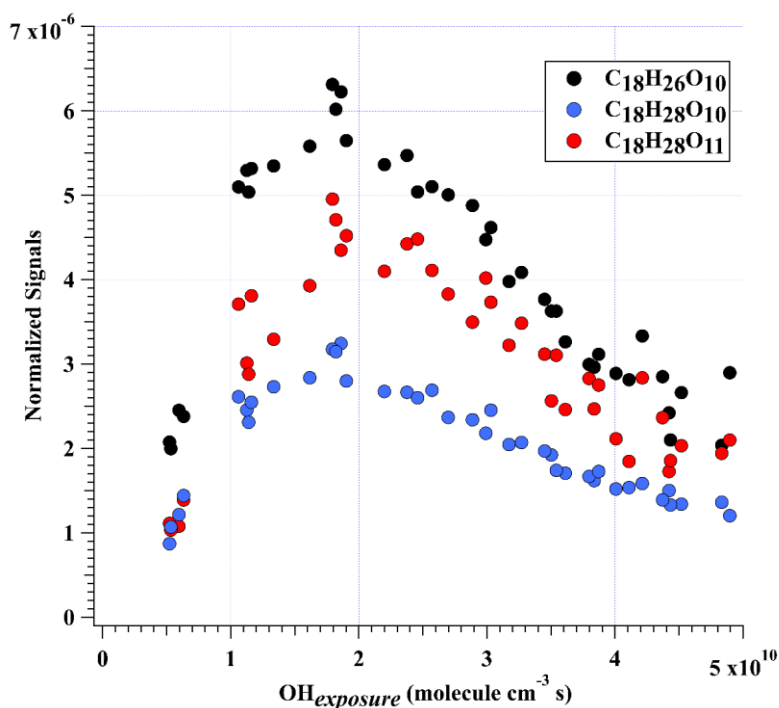
778 $C_{18}H_{26}O_{10}$ was characterized with the highest dimer signals for experiments with OH
779 exposures under 3.5×10^{10} molecule cm^{-3} s. Nevertheless, $C_{18}H_{26}O_{10}$, together with $C_{18}H_{28}O_{12}$,
780 $C_{18}H_{26}O_{12}$, $C_{18}H_{28}O_{11}$, $C_{18}H_{28}O_{13}$, and $C_{18}H_{28}O_{10}$ contributed more than 50% of total HOM
781 dimer signals at any OH exposure levels (Figure 2b). These six most abundant HOM dimers
782 correspond exactly to the hydroperoxyl, hydroxyl, and carbonyl termination products of
783 $C_{18}H_{27}O_{11}^{\bullet}$ and $C_{18}H_{27}O_{13}^{\bullet}$, respectively. These two RO_2 ($C_{18}H_{27}O_{11}^{\bullet}$ and $C_{18}H_{27}O_{13}^{\bullet}$), on the
784 other hand, could be generated by OH attacks to $C_{18}H_{26}O_8$ and $C_{18}H_{26}O_{10}$, respectively, which
785 strongly suggests the significant role of secondary OH chemistry in the formation of HOMs in
786 our experiments. In addition, $C_{18}H_{28}O_x$ can also be formed through accretion of a $C_9H_{13}O_m^{\bullet}$
787 radical and a $C_9H_{15}O_m^{\bullet}$ radical, as suggested by previous studies (Molteni et al., 2018;
788 Tsiliogiannis et al., 2019). However, since a $C_9H_{15}O_m^{\bullet}$ radical, as suggested by its hydrogen atom
789 number, can only be formed via an OH addition to the stabilized $C_9H_{14}O_m$ products through
790 multi-generation OH reactions, our conclusion that $C_{18}H_{28}O_x$ are multi-generation OH
791 oxidation products still holds. Figure 4 shows the normalized signals of these abundant HOM
792 dimers at different OH exposures.

793 (a)



794

795 (b)



796

797 **Figure 4.** Normalized signals of (a) $C_{18}H_{26}O_{12}$, $C_{18}H_{28}O_{12}$, and $C_{18}H_{28}O_{13}$, and (b) $C_{18}H_{26}O_{10}$,
 798 $C_{18}H_{28}O_{10}$, and $C_{18}H_{28}O_{11}$ measured at the exit of OFR in our high [OH] experiments without
 799 NO_x as a function of OH exposure.

800 This decrease of dimer at relatively high OH exposures are likely due to the accelerated
 801 accretion reactions in the OFR, resulted by the high RO_2 concentrations. The HOM dimers are
 802 formed earlier compared to under ambient conditions and then can go through the further
 803 oxidation reactions. Note that this does not mean the maximum concentrations of HOM dimers
 804 will also accurately occur at the same OH exposures in the atmosphere, because the detailed
 805 appearance time of the maximum concentrations of HOM dimers is dependent on their
 806 formation rate and loss rate. In our experiments, the formation rate and loss rate were not
 807 accelerated equally. On the other hand, the loss pathways of HOM dimers were not exactly the
 808 same as the ambient ~~due to the lack of aerosols in the OFR. With the decrease of particulate~~
 809 ~~pollution and thus condensation sinks in the polluted areas, the physical loss of HOMs might~~
 810 ~~be lower and the chemical process can be more important.~~ This series of experiments are not
 811 meant to specifically find out the detailed OH exposures when the maximum concentrations of
 812 HOM dimers will occur, but try to indicate how HOM dimers evolve with the increase of OH
 813 exposures. This work can be regarded as an indicator for the potential chemical fates of HOM
 814 dimers in the atmosphere if their survival time permitted. It should be noted that the gas-phase
 815 chemistry in the PAM OFR cannot be exactly the same as that in the ambient. Reactions of OH
 816 with OVOCs often lead to HO_2 formation, resulting in a $HO_2:RO_2$ ratio larger than 1 in the real
 817 atmosphere (Bianchi et al., 2019). A recent campaign conducted at a rural site in the Yangtze

818 River Delta estimated that the local ratio of HO₂:RO₂, the latter of which was presumably
819 derived from longer chain alkanes (> C₃), alkenes, and aromatic compounds, was around 1.66
820 (Ma et al., 2022). Such a high HO₂:RO₂ ratio condition is typically difficult to be simulated in
821 the laboratory experiments, as the precursors are usually hydrocarbons without any OVOCs
822 (Peng and Jimenez, 2020). This is exactly the case for our experiments, but its influences on
823 our conclusion were tiny, as have been discussed in the Section 3.1. Therefore, the difference
824 in the distribution of products will not change our conclusion.

825 Such an active secondary OH chemistry is consistent with the fast OH reaction rates of
826 HOMs. We take C₁₈H₂₆O₈ whose plausible structure is shown in **Figure S4** as an example,
827 which is the accretion product of two C₉H₁₃O₅[•]. Its OH reaction rate constant is estimated to be
828 around $2.07 \times 10^{-10} \text{ cm}^3 \text{ molecule}^{-1} \text{ s}^{-1}$ according to the structure-activity relationship (Jenkin et
829 al., 2018b, a), whose details are provided in Supplementary **Text S2S1**. This rate is several
830 times larger than that of 1,3,5-TMB, which enables a very active secondary OH chemistry in
831 the system. MCM recommended an OH reaction rate of $1.28 \times 10^{-10} \text{ cm}^3 \text{ molecule}^{-1} \text{ s}^{-1}$ for
832 TM135BPOOH (C₉H₁₄O₅) and $1.00 \times 10^{-10} \text{ cm}^3 \text{ molecule}^{-1} \text{ s}^{-1}$ for TM135OBPOH (C₉H₁₂O₄)
833 (Jenkin et al., 2003). The OH reaction rate for C₁₈H₂₆O₈ should also be fast due to the C=C
834 bonds in its structure, which is activated by the adjacent functionalities. Our calculation result
835 is consistent with this estimation.

836 The distributions of C18 organonitrates also verified the extensive secondary reactions.
837 The most abundant C18 organonitrate, C₁₈H₂₇NO₁₂ was a NO termination product of radical
838 C₁₈H₂₇O₁₁[•], which, as mentioned above, was the radical generated from the OH reaction with
839 C₁₈H₂₆O₈. C₁₈H₂₇NO₁₂ can also be formed either by accretion between a C₉H₁₅O_m[•] radical and
840 a C₉H₁₂NO_m[•] radical or accretion between a C₉H₁₃O_m[•] radical and a C₉H₁₄NO_m[•] radical. Both
841 C₉H₁₅O_m[•] and C₉H₁₄NO_m[•] radicals are a typical multi-generation RO₂ and thus prove
842 C₁₈H₂₇NO₁₂ is a multi-generation OH oxidation product. Other C18 organonitrates are believed
843 to be formed in a similar pathway. Hence, plenty of organonitrates have been formed via the
844 multi-generation OH reactions of first-generation stabilized products.

845 **3.3 Oxidation products in low [OH] experiments**

846 Given the larger sampling port, lower initial ozone concentrations, lower UV light
847 intensities, and a better performance of mass spectrometer in this series of low [OH]
848 experiments, a number of new species were detected in the 2nd-round experiments, including
849 three typical termination reaction products of BPR, i.e., C₉H₁₄O₄, C₉H₁₄O₅, and C₉H₁₃NO₆, and
850 a number of low volatile compounds, e.g., C₉H_xO₁₁ ($x = 12 - 15$). The distributions of oxidation
851 products detected by nitrate CI-TOF in Exp. 2-3, 2-4, and 2-7, representative low [OH]

852 experiments, are displayed in [Figure 5](#). The detailed molecular formula and their contributions
853 to total HOMs signals are provided in [Tables S6](#) and [S7](#).

854 In addition, certain C9 and C18 HOMs with lower DBE than typical first-generation
855 products predicted by MCM (Saunders et al., 2003) or reported by previous studies (Berndt et
856 al., 2018b), were detected in Exp. 2-3, 2-4, and 2-7, although [OH] in these experiments are
857 much lower than those in the 1st-round experiments.

858 Observation of compounds with lower DBE in Exp. 2-3, 2-4, and 2-7 including HOM
859 monomers with DBE lower than 3 and HOM dimers with DBE lower than 6, as well as
860 monomer radicals with DBE lower than 3 including $C_9H_{15}O_m\cdot$ ($m = 7 - 11$) and $C_9H_{14}NO_9\cdot$,
861 proves the re-initiation of OH oxidation of the stabilized products in experiments with
862 atmospheric relevant [OH]. All the stabilized products and radicals depicted in the proposed
863 mechanisms ([Scheme 2](#) and [Scheme 3](#)) were detected in both Exp. 2-3 and Exp. 2-4, except for
864 $C_9H_{15}O_9\cdot$ that was only detected in Exp. 2-3. This means that the proposed reaction pathways
865 have already happened under atmospheric [OH] conditions with limited OH exposures.
866 However, as we do not know the exact structures of these OOMs and radicals, the proposed
867 reaction pathways are merely based on the chemical formulae detected by nitrate CIMS and
868 nitrate CI-TOF and proposed according to the general mechanisms of OH addition reactions to
869 the C=C bond. Other reaction pathways to generate these compounds or other isomers
870 generated in these pathways are undoubtedly feasible.

871 A lot of compounds detected in the experiments without NO_x were not observed in [the](#)
872 counterpart experiments with NO_x. We also did not detect decent signals of HOM dimers in the
873 NO_x-present experiments in the 2nd-round experiments. [Such a dramatic decrease in the](#)
874 [abundance of HOM dimers after the introduction of NO_x into the aromatic oxidation system](#)
875 [has been reported in several previous studies](#) (Garmash et al., 2020; Wang et al., 2020b;
876 Tsiligiannis et al., 2019). This might come from the dominant significance of NO + RO₂
877 reactions ([R8 - R9](#)) after the introduction of NO_x into system, making signals of certain HOMs
878 from other channels lower than the detection limit of the instrument. The proportions of other
879 reaction channels decreased, and were reassigned to the NO channel, as evidenced by the fact
880 that most of observed oxidation products were organonitrates, which is in an excellent
881 agreement with the modeled channel proportions in Section 3.1.

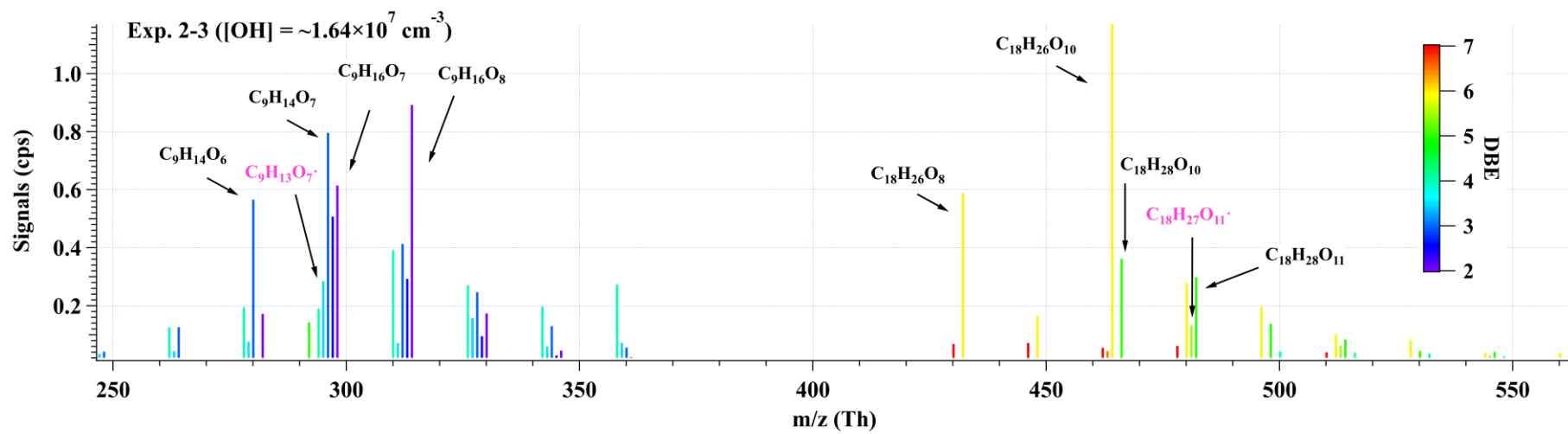
882 Many organonitrates were observed in both series of experiments. In the low [OH]
883 experiments, the most significant compound was $C_9H_{13}NO_8$, whose formula matches the NO
884 termination product of $C_9H_{13}O_7\cdot$, i.e., autoxidation product of BPR. The second most important
885 compound, $C_9H_{14}N_2O_{10}$ in our low [OH] experiments, was the most significant product in the
886 high [OH] experiments in presence of NO_x, whose formula matches the NO termination product

887 of $C_9H_{14}NO_9\cdot$, i.e., the RO_2 formed via an OH addition to $C_9H_{13}NO_6$, the NO termination
888 product of BPR. All of the products and radicals mentioned above were observed in Exp. 2-7,
889 as shown in **Figure 5c**. From the perspective of molecular formula, $C_9H_{14}N_2O_{10}$ is also one of
890 the most frequently observed multi-nitrogen-containing compound in polluted atmospheres,
891 whose seasonal variations show a good correlation with [OH] (Guo et al., 2022; Yang et al.,
892 2023).

893 A comparison of relative abundances of C9 and C18 products under different [OH] levels
894 is helpful for the elucidation of their formation pathways. The difference in product
895 distributions between Exp. 2-3 ([OH] = $\sim 1.69 \times 10^7$ molecule cm^{-3}) and Exp. 2-1 ([OH] =
896 $\sim 1.03 \times 10^8$ molecule cm^{-3}), as well as between Exp. 2-3 and Exp. 1-12 ([OH] = $\sim 8.47 \times 10^8$
897 molecule cm^{-3}) is shown in **Figure 6**. The normalized abundance was obtained by normalizing
898 all the products to the most abundant one in each experiment, i.e., $C_{18}H_{26}O_{10}$ in Exp. 2-1 and
899 Exp. 2-3, and $C_9H_{14}O_7$ in Exp. 1-12. The changes in the normalized abundance were obtained
900 by subtracting the normalized abundance in Exp. 2-1 from that in Exp. 2-3, and Exp. 1-12 from
901 Exp. 2-3. As the [OH] and OH exposure increased, there was a noticeable rise in the relative
902 abundance of more oxygenated compounds, which can be attributed to the more-intensive/larger
903 proportion of multi-generation OH oxidation in high OH exposure experiments. This
904 comparison demonstrates the capacity and potential of multi-generation OH oxidation to reduce
905 DBE and elevate the oxygenated levels of oxidation products.

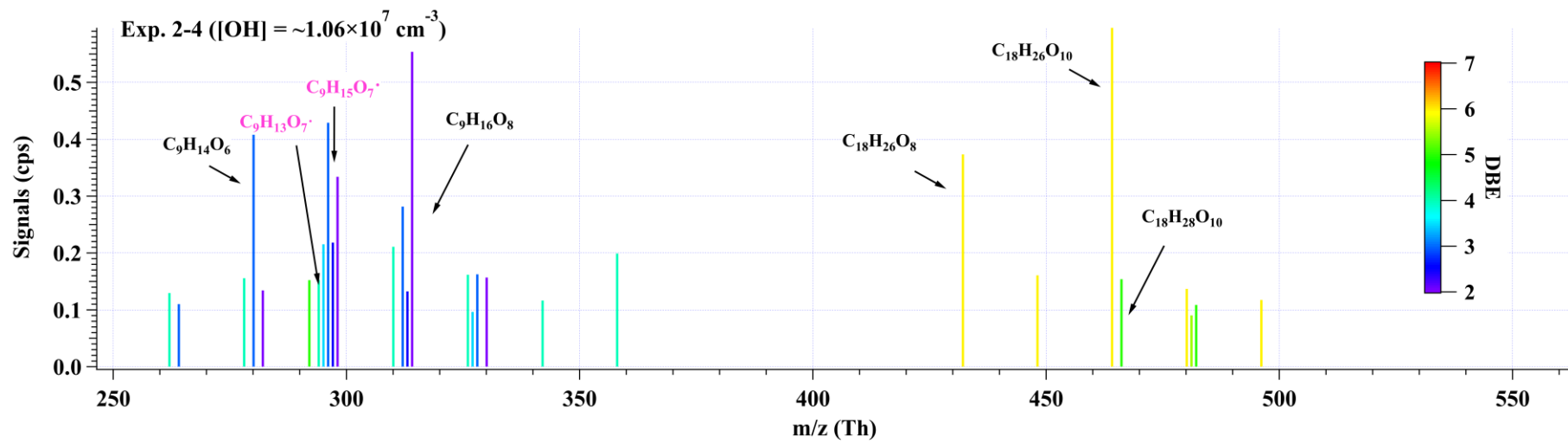
906 In conclusion, observation of the same low DBE compounds, i.e., DBE = 2, in both low
907 [OH] and high [OH] experiments confirms the feasibility of the generation of HOMs under
908 atmospheric relevant conditions. The detection of $C_9H_{14}O_5$, $C_9H_{15}O_8\cdot$, $C_9H_{14}O_7$, $C_9H_{14}O_8$,
909 $C_9H_{15}O_7\cdot$, and $C_9H_{16}O_8$, and $C_9H_{14}O_6$, $C_9H_{15}O_9\cdot$, $C_9H_{14}O_8$, $C_9H_{14}O_9$, $C_9H_{15}O_8\cdot$, and $C_9H_{16}O_9$, in
910 low [OH] experiments also confirms the potential existence of the proposed mechanisms, i.e.,
911 Scheme 2 and Scheme 3, respectively. Certainly, other potential formation pathways for these
912 products are possible.

913 (a)



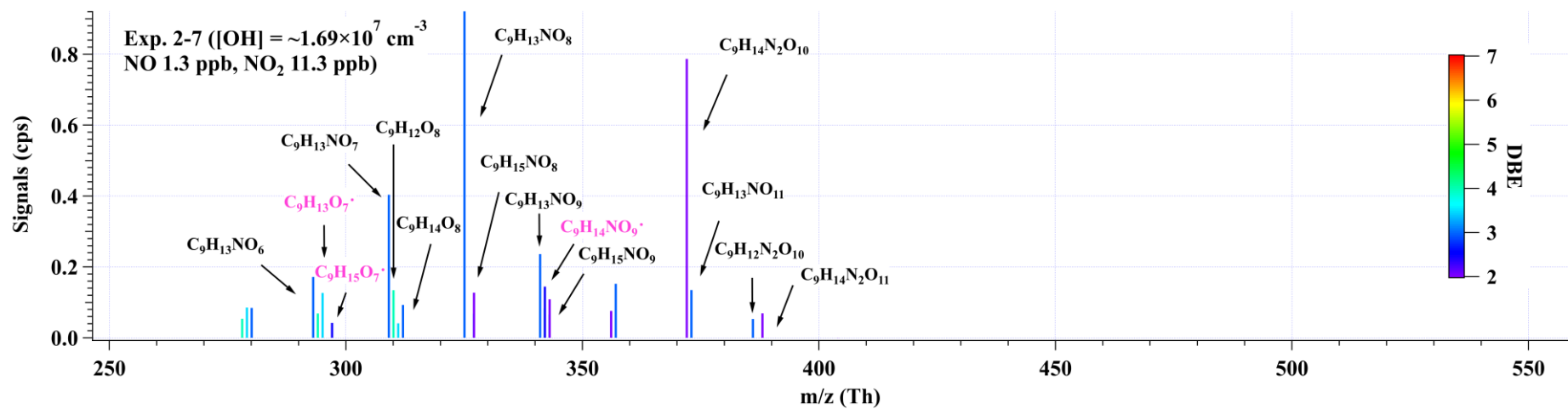
914

915 (b)



916

917 (c)



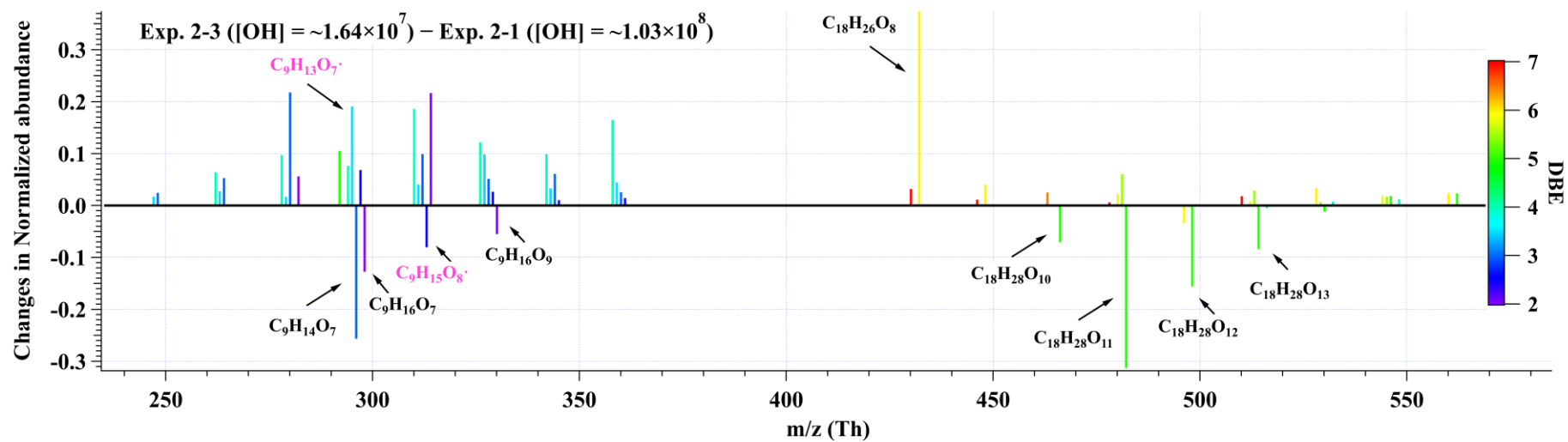
918
919

920 **Figure 5.** Distributions of C9 and C18 products detected by nitrate CI-TOF in (a) Exp. 2-3, (b) Exp. 2-4, and (c) Exp. 2-7. The reagent ion, NO₃⁻, is omitted in
921 the label for the molecular formula. Important radicals were labelled in pink. Note that no convinced signals of HOM dimers were observed in the 2nd-round
922 experiments with NO_x.

923

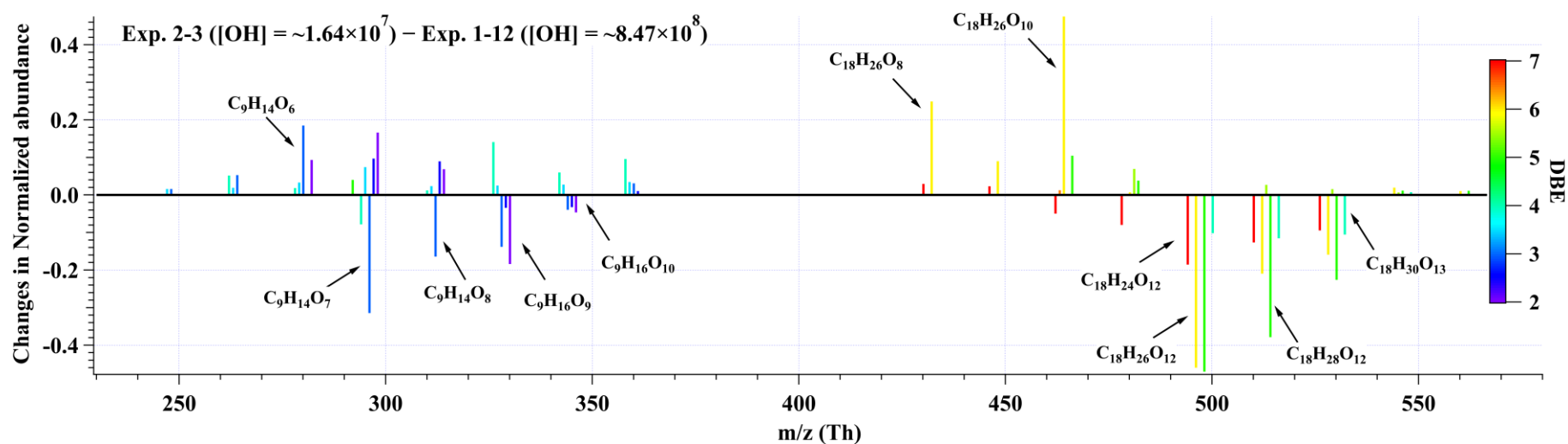
924

925 (a)



926

927 (b)



928

929 **Figure 6.** The changes in normalized abundance of C9 and C18 products observed by nitrate CI-TOF in (a) Exp.2-3 relative to Exp.2-1, and (b) Exp.2-3 relative to Exp.1-12. The reagent ion, NO_3^- , is omitted in the label. The normalized abundance was obtained by normalizing all the products to the most abundant one in each experiment, i.e., $C_{18}H_{26}O_{10}$ in Exp.2-1 and Exp.2-3, and $C_9H_{14}O_7$ in Exp.1-12.

930

931

932 **4 Atmospheric Implications**

933 This study highlights the influences of OH exposure on the distribution and evolution of
934 1,3,5-TMB-derived HOMs. Secondary OH reactions can influence HOMs' composition by
935 directly reacting with the stabilized first-generation oxidation products, leading to enhanced
936 formation of HOMs, if the stabilized, first-generation oxidation products could survive from
937 condensation loss onto pre-existing particles. Observation of organonitrates generated in the
938 NO experiments further confirmed the secondary OH oxidation. Due to the elevated abundance
939 and the reduced volatility of HOMs, growth rates of newly formed nanoparticles in the presence
940 of HOMs could be raised, especially in high-OH environments, which prevails in the summer
941 noon. Substantially high concentrations of OH have been frequently observed in polluted
942 environments during summer, e.g., megacities in China (Tan et al., 2019), and thus more active
943 secondary OH reactions are expected compared to wintertime. As a plausible consequence,
944 seasonal differences of HOMs and new particle formation (NPF) are resulted (Qiao et al., 2021;
945 Yao et al., 2018; Guo et al., 2022). Furthermore, previous studies suggest that high
946 concentrations of NO can suppress the formation of HOMs via the suppression of autoxidation
947 (Pye et al., 2019), but the influences of such a suppression could have been overestimated, since
948 secondary OH reactions can continue to oxidize the stabilized organonitrates. Our conclusions
949 help to explain the existing gap between model prediction and ambient measurement on the
950 HOMs concentrations (Qi et al., 2018), and to build a global HOMs simulation model.

951

952 *Data availability.* Data used in this work are available upon request from the corresponding
953 authors.

954

955 *Supplement.* The supplement related to this article is available online.

956

957 *Author contributions.* LW and Yuwei Wang designed the experiments. Yuwei Wang [and](#)
958 [Chuang Li](#) conducted the laboratory experiments. Yuwei Wang analyzed the data. Yuwei Wang
959 and LW wrote the paper. All co-authors discussed the results and commented on the manuscript.

960

961 *Competing interests.* The authors declare that they have no conflict of interest.

962

963 *Acknowledgments.* This work was financially supported by the National Natural Science
964 Foundation of China (21925601, 22127811). The authors declare no competing interests.

965 Yuwei Wang would like to thank Andrew T. Lambe, Peng Zhe, and Jose Jimenez for helpful
966 discussions on PAM experiments.

967 **References**

- 968 Assaf, E., Song, B., Tomas, A., Schoemaeker, C., and Fittschen, C.: Rate Constant of the
969 Reaction between CH₃O₂ Radicals and OH Radicals Revisited, *J. Phys. Chem. A*, 120,
970 8923–8932, <https://doi.org/10.1021/acs.jpca.6b07704>, 2016.
- 971 Assaf, E., Tanaka, S., Kajii, Y., Schoemaeker, C., and Fittschen, C.: Rate constants of the
972 reaction of C₂–C₄ peroxy radicals with OH radicals, *Chem. Phys. Lett.*, 684, 245–249,
973 <https://doi.org/10.1016/j.cplett.2017.06.062>, 2017.
- 974 Berndt, T., Mentler, B., Scholz, W., Fischer, L., Herrmann, H., Kulmala, M., and Hansel, A.:
975 Accretion Product Formation from Ozonolysis and OH Radical Reaction of α -Pinene:
976 Mechanistic Insight and the Influence of Isoprene and Ethylene, *Environ. Sci. Technol.*, 52,
977 11069–11077, <https://doi.org/10.1021/acs.est.8b02210>, 2018a.
- 978 Berndt, T., Scholz, W., Mentler, B., Fischer, L., Herrmann, H., Kulmala, M., and Hansel, A.:
979 Accretion Product Formation from Self- and Cross-Reactions of RO₂ Radicals in the
980 Atmosphere, *Angew. Chemie - Int. Ed.*, 57, 3820–3824,
981 <https://doi.org/10.1002/anie.201710989>, 2018b.
- 982 Bianchi, F., Kurtén, T., Riva, M., Mohr, C., Rissanen, M. P., Roldin, P., Berndt, T., Crounse,
983 J. D., Wennberg, P. O., Mentel, T. F., Wildt, J., Junninen, H., Jokinen, T., Kulmala, M.,
984 Worsnop, D. R., Thornton, J. A., Donahue, N., Kjaergaard, H. G., and Ehn, M.: Highly
985 Oxygenated Organic Molecules (HOM) from Gas-Phase Autoxidation Involving Peroxy
986 Radicals: A Key Contributor to Atmospheric Aerosol, *Chem. Rev.*, 119, 3472–3509,
987 <https://doi.org/10.1021/acs.chemrev.8b00395>, 2019.
- 988 Bossolasco, A., Faragó, E. P., Schoemaeker, C., and Fittschen, C.: Rate constant of the
989 reaction between CH₃O₂ and OH radicals, *Chem. Phys. Lett.*, 593, 7–13,
990 <https://doi.org/10.1016/j.cplett.2013.12.052>, 2014.
- 991 Brune, W. H.: The Chamber Wall Index for Gas-Wall Interactions in Atmospheric
992 Environmental Enclosures, *Environ. Sci. Technol.*, 53, 3645–3652,
993 <https://doi.org/10.1021/acs.est.8b06260>, 2019.
- 994 Caravan, R. L., Khan, M. A. H., Zádor, J., Sheps, L., Antonov, I. O., Rotavera, B.,
995 Ramasesha, K., Au, K., Chen, M. W., Rösch, D., Osborn, D. L., Fittschen, C., Schoemaeker,
996 C., Duncianu, M., Grira, A., Dusanter, S., Tomas, A., Percival, C. J., Shallcross, D. E., and
997 Taatjes, C. A.: The reaction of hydroxyl and methylperoxy radicals is not a major source of
998 atmospheric methanol, *Nat. Commun.*, 9, 1–9, <https://doi.org/10.1038/s41467-018-06716-x>,
999 2018.
- 1000 Cheng, X., Chen, Q., Li, Y. J., Zheng, Y., Liao, K., and Huang, G.: Highly Oxygenated
1001 Organic Molecules Produced by the Oxidation of Benzene and Toluene in a Wide Range of
1002 OH Exposure and NO_x Conditions, *Atmos. Chem. Phys.*, 1–23, [https://doi.org/10.5194/acp-](https://doi.org/10.5194/acp-2021-201)
1003 2021-201, 2021.
- 1004 Crounse, J. D., Nielsen, L. B., Jørgensen, S., Kjaergaard, H. G., and Wennberg, P. O.:
1005 Autoxidation of organic compounds in the atmosphere, *J. Phys. Chem. Lett.*, 4, 3513–3520,
1006 <https://doi.org/10.1021/jz4019207>, 2013.
- 1007 Deng, C., Fu, Y., Dada, L., Yan, C., Cai, R., Yang, D., Zhou, Y., Yin, R., Lu, Y., Li, X., Qiao,
1008 X., Fan, X., Nie, W., Kontkanen, J., Kangasluoma, J., Chu, B., Ding, A., Kerminen, V. M.,
1009 Paasonen, P., Worsnop, D. R., Bianchi, F., Liu, Y., Zheng, J., Wang, L., Kulmala, M., and

1010 Jiang, J.: Seasonal characteristics of new particle formation and growth in urban Beijing,
1011 *Environ. Sci. Technol.*, 54, 8547–8557, <https://doi.org/10.1021/acs.est.0c00808>, 2020.

1012 Ehn, M., Thornton, J. A., Kleist, E., Sipilä, M., Junninen, H., Pullinen, I., Springer, M.,
1013 Rubach, F., Tillmann, R., Lee, B., Lopez-Hilfiker, F., Andres, S., Acir, I. H., Rissanen, M.,
1014 Jokinen, T., Schobesberger, S., Kangasluoma, J., Kontkanen, J., Nieminen, T., Kurtén, T.,
1015 Nielsen, L. B., Jørgensen, S., Kjaergaard, H. G., Canagaratna, M., Maso, M. D., Berndt, T.,
1016 Petäjä, T., Wahner, A., Kerminen, V. M., Kulmala, M., Worsnop, D. R., Wildt, J., and
1017 Mentel, T. F.: A large source of low-volatility secondary organic aerosol, *Nature*, 506, 476–
1018 479, <https://doi.org/10.1038/nature13032>, 2014.

1019 Eisele, F. L. and Tanner, D. J.: Measurement of the gas phase concentration of H₂SO₄ and
1020 methane sulfonic acid and estimates of H₂SO₄ production and loss in the atmosphere, *J.*
1021 *Geophys. Res. Atmos.*, 98, 9001–9010, <https://doi.org/10.1029/93JD00031>, 1993.

1022 Fittschen, C.: The reaction of peroxy radicals with OH radicals, *Chem. Phys. Lett.*, 725, 102–
1023 108, <https://doi.org/10.1016/j.cplett.2019.04.002>, 2019.

1024 Fuller, E. N., Schettler, P. D., and Giddings, J. C.: A new method for prediction of binary gas-
1025 phase diffusion coefficients, *Ind. Eng. Chem.*, 58, 18–27,
1026 <https://doi.org/10.1021/ie50677a007>, 1966.

1027 Garmash, O., Rissanen, M. P., Pullinen, I., Schmitt, S., Kausiala, O., Tillmann, R., Zhao, D.,
1028 Percival, C., Bannan, T. J., Priestley, M., Hallquist, Å. M., Kleist, E., Kiendler-Scharr, A.,
1029 Hallquist, M., Berndt, T., McFiggans, G., Wildt, J., Mentel, T. F., and Ehn, M.: Multi-
1030 generation OH oxidation as a source for highly oxygenated organic molecules from
1031 aromatics, *Atmos. Chem. Phys.*, 20, 515–537, <https://doi.org/10.5194/acp-20-515-2020>, 2020.

1032 Guo, Y., Yan, C., Liu, Y., Qiao, X., Zheng, F., Zhang, Y., Zhou, Y., Li, C., Fan, X., Lin, Z.,
1033 Feng, Z., Zhang, Y., Zheng, P., Tian, L., Nie, W., Wang, Z., Huang, D., Daellenbach, K. R.,
1034 Yao, L., Dada, L., Bianchi, F., Jiang, J., Liu, Y., Kerminen, V. M., and Kulmala, M.: Seasonal
1035 variation in oxygenated organic molecules in urban Beijing and their contribution to
1036 secondary organic aerosol, *Atmos. Chem. Phys.*, 22, 10077–10097,
1037 <https://doi.org/10.5194/acp-22-10077-2022>, 2022.

1038 Heinritzi, M., Simon, M., Steiner, G., Wagner, A. C., Kürten, A., Hansel, A., and Curtius, J.:
1039 Characterization of the mass-dependent transmission efficiency of a CIMS, *Atmos. Meas.*
1040 *Tech.*, 9, 1449–1460, <https://doi.org/10.5194/amt-9-1449-2016>, 2016.

1041 Hyttinen, N., Kupiainen-Määttä, O., Rissanen, M. P., Muuronen, M., Ehn, M., and Kurtén, T.:
1042 Modeling the Charging of Highly Oxidized Cyclohexene Ozonolysis Products Using Nitrate-
1043 Based Chemical Ionization, *J. Phys. Chem. A*, 119, 6339–6345,
1044 <https://doi.org/10.1021/acs.jpca.5b01818>, 2015.

1045 Iyer, S., Kumar, A., Savolainen, A., Barua, S., Daub, C., Pichelstorfer, L., Roldin, P.,
1046 Garmash, O., Seal, P., Kurtén, T., and Rissanen, M.: Molecular rearrangement of bicyclic
1047 peroxy radicals is a key route to aerosol from aromatics, *Nat. Commun.*, 14, 4984,
1048 <https://doi.org/10.1038/s41467-023-40675-2>, 2023.

1049 Jacob, D. J.: *Introduction to atmospheric chemistry*, Princeton, 1999.

1050 Jenkin, M. E., Saunders, S. M., Wagner, V., and Pilling, M. J.: Protocol for the development
1051 of the Master Chemical Mechanism, MCM v3 (Part B): tropospheric degradation of aromatic
1052 volatile organic compounds, *Atmos. Chem. Phys.*, 3, 181–193, [https://doi.org/10.5194/acp-3-](https://doi.org/10.5194/acp-3-181-2003)
1053 181-2003, 2003.

1054 Jenkin, M. E., Valorso, R., Aumont, B., Rickard, A. R., and Wallington, T. J.: Estimation of
1055 rate coefficients and branching ratios for gas-phase reactions of OH with aliphatic organic
1056 compounds for use in automated mechanism construction, 9297–9328 pp.,
1057 <https://doi.org/10.5194/acp-18-9297-2018>, 2018a.

1058 Jenkin, M. E., Valorso, R., Aumont, B., Rickard, A. R., and Wallington, T. J.: Estimation of
1059 rate coefficients and branching ratios for gas-phase reactions of OH with aromatic organic
1060 compounds for use in automated mechanism construction, *Atmos. Chem. Phys.*, 18, 9329–
1061 9349, <https://doi.org/10.5194/acp-18-9329-2018>, 2018b.

1062 Keller-Rudek, H., Moortgat, G. K., Sander, R., and Sørensen, R.: The MPI-Mainz UV/VIS
1063 spectral atlas of gaseous molecules of atmospheric interest, *Earth Syst. Sci. Data*, 5, 365–373,
1064 <https://doi.org/10.5194/essd-5-365-2013>, 2013.

1065 Knap, H. C. and Jørgensen, S.: Rapid Hydrogen Shift Reactions in Acyl Peroxy Radicals, *J.*
1066 *Phys. Chem. A*, 121, 1470–1479, <https://doi.org/10.1021/acs.jpca.6b12787>, 2017.

1067 Krechmer, J., Lopez-Hilfiker, F., Koss, A., Hutterli, M., Stoermer, C., Deming, B., Kimmel,
1068 J., Warneke, C., Holzinger, R., Jayne, J., Worsnop, D., Fuhrer, K., Gonin, M., and De Gouw,
1069 J.: Evaluation of a New Reagent-Ion Source and Focusing Ion– Molecule Reactor for Use in
1070 Proton-Transfer-Reaction Mass Spectrometry, *Anal. Chem.*, 90, 12011–12018,
1071 <https://doi.org/10.1021/acs.analchem.8b02641>, 2018.

1072 Lambe, A., Massoli, P., Zhang, X., Canagaratna, M., Nowak, J., Daube, C., Yan, C., Nie, W.,
1073 Onasch, T., Jayne, J., Kolb, C., Davidovits, P., Worsnop, D., and Brune, W.: Controlled nitric
1074 oxide production via O(1D) + N₂O reactions for use in oxidation flow reactor studies, *Atmos.*
1075 *Meas. Tech.*, 10, 2283–2298, <https://doi.org/10.5194/amt-10-2283-2017>, 2017.

1076 Lambe, A., Krechmer, J., Peng, Z., Casar, J., Carrasquillo, A., Raff, J., Jimenez, J., and
1077 Worsnop, D.: HO_x and NO_x production in oxidation flow reactors via photolysis of, 1–22,
1078 2018.

1079 Lambe, A. T., Ahern, A. T., Williams, L. R., Slowik, J. G., Wong, J. P. S., Abbatt, J. P. D.,
1080 Brune, W. H., Ng, N. L., Wright, J. P., Croasdale, D. R., Worsnop, D. R., Davidovits, P., and
1081 Onasch, T. B.: Characterization of aerosol photooxidation flow reactors: heterogeneous
1082 oxidation, secondary organic aerosol formation and cloud condensation nuclei activity
1083 measurements, *Atmos. Meas. Tech.*, 4, 445–461, <https://doi.org/10.5194/amt-4-445-2011>,
1084 2011.

1085 Lambe, A. T., Chhabra, P. S., Onasch, T. B., Brune, W. H., Hunter, J. F., Kroll, J. H.,
1086 Cummings, M. J., Brogan, J. F., Parmar, Y., Worsnop, D. R., Kolb, C. E., and Davidovits, P.:
1087 Effect of oxidant concentration, exposure time, and seed particles on secondary organic
1088 aerosol chemical composition and yield, *Atmos. Chem. Phys.*, 15, 3063–3075,
1089 <https://doi.org/10.5194/acp-15-3063-2015>, 2015.

1090 Lehtipalo, K., Yan, C., Dada, L., Bianchi, F., Xiao, M., Wagner, R., Stolzenburg, D., Ahonen,
1091 L. R., Amorim, A., Baccarini, A., Bauer, P. S., Baumgartner, B., Bergen, A., Bernhammer, A.
1092 K., Breitenlechner, M., Brilke, S., Buchholz, A., Mazon, S. B., Chen, D., Chen, X., Dias, A.,
1093 Dommen, J., Draper, D. C., Duplissy, J., Ehn, M., Finkenzeller, H., Fischer, L., Frege, C.,
1094 Fuchs, C., Garmash, O., Gordon, H., Hakala, J., He, X., Heikkinen, L., Heinritzi, M., Helm, J.
1095 C., Hofbauer, V., Hoyle, C. R., Jokinen, T., Kangasluoma, J., Kerminen, V. M., Kim, C.,
1096 Kirkby, J., Kontkanen, J., Kürten, A., Lawler, M. J., Mai, H., Mathot, S., Mauldin, R. L.,
1097 Molteni, U., Nie, W., Nieminen, T., Ojdanic, A., Onnela, A., Passananti, M.,

1098 Petäjä, T., Piel, F., Pospisilova, V., Quéléver, L. L. J., Rissanen, M. P., Rose, C., Sarnela, N.,
1099 Schallhart, S., Schuchmann, S., Sengupta, K., Simon, M., Sipilä, M., Tauber, C., Tomé, A.,
1100 Tröstl, J., Väisänen, O., Vogel, A. L., Volkamer, R., Wagner, A. C., Wang, M., Weitz, L.,
1101 Wimmer, D., Ye, P., Ylisirniö, A., Zha, Q., Carslaw, K. S., Curtius, J., Donahue, N. M.,
1102 Flagan, R. C., Hansel, A., Riipinen, I., Virtanen, A., Winkler, P. M., Baltensperger, U.,
1103 Kulmala, M., and Worsnop, D. R.: Multicomponent new particle formation from sulfuric
1104 acid, ammonia, and biogenic vapors, *Sci. Adv.*, 4, 1–10,
1105 <https://doi.org/10.1126/sciadv.aau5363>, 2018.

1106 Li, R., Palm, B. B., Ortega, A. M., Hlywiak, J., Hu, W., Peng, Z., Day, D. A., Knote, C.,
1107 Brune, W. H., De Gouw, J. A., and Jimenez, J. L.: Modeling the radical chemistry in an
1108 oxidation flow reactor: Radical formation and recycling, sensitivities, and the OH exposure
1109 estimation equation, *J. Phys. Chem. A*, 119, 4418–4432, <https://doi.org/10.1021/jp509534k>,
1110 2015.

1111 Lu, K. D., Rohrer, F., Holland, F., Fuchs, H., Bohn, B., Brauers, T., Chang, C. C., Häsel, R.,
1112 Hu, M., Kita, K., Kondo, Y., Li, X., Lou, S. R., Nehr, S., Shao, M., Zeng, L. M., Wahner, A.,
1113 Zhang, Y. H., and Hofzumahaus, A.: Observation and modelling of OH and HO₂
1114 concentrations in the Pearl River Delta 2006: A missing OH source in a VOC rich
1115 atmosphere, *Atmos. Chem. Phys.*, 12, 1541–1569, <https://doi.org/10.5194/acp-12-1541-2012>,
1116 2012.

1117 Ma, X., Tan, Z., Lu, K., Yang, X., Chen, X., Wang, H., Chen, S., Fang, X., Li, S., Li, X., Liu,
1118 J., Liu, Y., Lou, S., Qiu, W., Wang, H., Zeng, L., and Zhang, Y.: OH and HO₂ radical
1119 chemistry at a suburban site during the EXPLORE-YRD campaign in 2018, *Atmos. Chem.*
1120 *Phys.*, 22, 7005–7028, <https://doi.org/10.5194/acp-22-7005-2022>, 2022.

1121 McMurtry, P. H. and Grosjean, D.: Gas and Aerosol Wall Losses in Teflon Film Smog
1122 Chambers, *Environ. Sci. Technol.*, 19, 1176–1182, <https://doi.org/10.1021/es00142a006>,
1123 1985.

1124 Mehra, A., Wang, Y., E. Krechmer, J., Lambe, A., Majluf, F., A. Morris, M., Priestley, M., J.
1125 Bannan, T., J. Bryant, D., L. Pereira, K., F. Hamilton, J., R. Rickard, A., J. Newland, M.,
1126 Stark, H., Croteau, P., T. Jayne, J., R. Worsnop, D., R. Canagaratna, M., Wang, L., and Coe,
1127 H.: Evaluation of the chemical composition of gas- And particle-phase products of aromatic
1128 oxidation, *Atmos. Chem. Phys.*, 20, 9783–9803, <https://doi.org/10.5194/acp-20-9783-2020>,
1129 2020.

1130 Mentel, T. F., Springer, M., Ehn, M., Kleist, E., Pullinen, I., Kurtén, T., Rissanen, M.,
1131 Wahner, A., and Wildt, J.: Formation of highly oxidized multifunctional compounds:
1132 Autoxidation of peroxy radicals formed in the ozonolysis of alkenes - Deduced from
1133 structure-product relationships, *Atmos. Chem. Phys.*, 15, 6745–6765,
1134 <https://doi.org/10.5194/acp-15-6745-2015>, 2015.

1135 Mohr, C., Thornton, J. A., Heitto, A., Lopez-hil, F. D., Lutz, A., Riipinen, I., Hong, J.,
1136 Donahue, N. M., Hallquist, M., Petäjä, T., Kulmala, M., and Yli-juuti, T.: Molecular
1137 identification of organic vapors driving atmospheric nanoparticle growth, *Nat. Commun.*, 1–
1138 7, <https://doi.org/10.1038/s41467-019-12473-2>, 2019.

1139 Molteni, U., Bianchi, F., Klein, F., Haddad, I. El, Frege, C., Rossi, M. J., Dommen, J., and
1140 Baltensperger, U.: Formation of highly oxygenated organic molecules from aromatic

1141 compounds, *Atmos. Chem. Phys.*, 18, 1909–1921, <https://doi.org/10.5194/acp-18-1909-2018>,
1142 2018.

1143 Müller, J. F., Liu, Z., Nguyen, V. S., Stavrou, T., Harvey, J. N., and Peeters, J.: The
1144 reaction of methyl peroxy and hydroxyl radicals as a major source of atmospheric methanol,
1145 *Nat. Commun.*, 7, 1–11, <https://doi.org/10.1038/ncomms13213>, 2016.

1146 Ng, N. L., Canagaratna, M. R., Zhang, Q., Jimenez, J. L., Tian, J., Ulbrich, I. M., Kroll, J. H.,
1147 Docherty, K. S., Chhabra, P. S., Bahreini, R., Murphy, S. M., Seinfeld, J. H., Hildebrandt, L.,
1148 Donahue, N. M., Decarlo, P. F., Lanz, V. A., Prévôt, A. S. H., Dinar, E., Rudich, Y., and
1149 Worsnop, D. R.: Organic aerosol components observed in Northern Hemispheric datasets
1150 from Aerosol Mass Spectrometry, *Atmos. Chem. Phys.*, 10, 4625–4641,
1151 <https://doi.org/10.5194/acp-10-4625-2010>, 2010.

1152 Orlando, J. J. and Tyndall, G. S.: Laboratory studies of organic peroxy radical chemistry: An
1153 overview with emphasis on recent issues of atmospheric significance, *Chem. Soc. Rev.*, 41,
1154 6294–6317, <https://doi.org/10.1039/c2cs35166h>, 2012.

1155 Otkjær, R. V., Jakobsen, H. H., Tram, C. M., and Kjaergaard, H. G.: Calculated Hydrogen
1156 Shift Rate Constants in Substituted Alkyl Peroxy Radicals, *J. Phys. Chem. A*, 122, 8665–
1157 8673, <https://doi.org/10.1021/acs.jpca.8b06223>, 2018.

1158 Palm, B. B., Campuzano-Jost, P., Ortega, A. M., Day, D. A., Kaser, L., Jud, W., Karl, T.,
1159 Hansel, A., Hunter, J. F., Cross, E. S., Kroll, J. H., Peng, Z., Brune, W. H., and Jimenez, J. L.:
1160 In situ secondary organic aerosol formation from ambient pine forest air using an oxidation
1161 flow reactor, *Atmos. Chem. Phys.*, 16, 2943–2970, <https://doi.org/10.5194/acp-16-2943-2016>,
1162 2016.

1163 Peng, Z. and Jimenez, J. L.: Radical chemistry in oxidation flow reactors for atmospheric
1164 chemistry research, *Chem. Soc. Rev.*, 49, 2570–2616, <https://doi.org/10.1039/c9cs00766k>,
1165 2020.

1166 Peng, Z., Day, D. A., Ortega, A. M., Palm, B. B., Hu, W., Stark, H., Li, R., Tsigaridis, K.,
1167 Brune, W. H., and Jimenez, J. L.: Non-OH chemistry in oxidation flow reactors for the study
1168 of atmospheric chemistry systematically examined by modeling, *Atmos. Chem. Phys.*, 16,
1169 4283–4305, <https://doi.org/10.5194/acp-16-4283-2016>, 2016.

1170 Praske, E., Otkjær, R. V., Crouse, J. D., Hethcox, J. C., Stoltz, B. M., Kjaergaard, H. G., and
1171 Wennberg, P. O.: Atmospheric autoxidation is increasingly important in urban and suburban
1172 North America, *Proc. Natl. Acad. Sci. U. S. A.*, 115, 64–69,
1173 <https://doi.org/10.1073/pnas.1715540115>, 2018.

1174 Pye, H. O. T., D'Ambro, E. L., Lee, B. H., Schobesberger, S., Takeuchi, M., Zhao, Y., Lopez-
1175 Hilfiker, F., Liu, J., Shilling, J. E., Xing, J., Mathur, R., Middlebrook, A. M., Liao, J., Welti,
1176 A., Graus, M., Warneke, C., de Gouw, J. A., Holloway, J. S., Ryerson, T. B., Pollack, I. B.,
1177 and Thornton, J. A.: Anthropogenic enhancements to production of highly oxygenated
1178 molecules from autoxidation, *Proc. Natl. Acad. Sci. U. S. A.*, 116, 6641–6646,
1179 <https://doi.org/10.1073/pnas.1810774116>, 2019.

1180 Qi, X., Ding, A., Roldin, P., Xu, Z., Zhou, P., Sarnela, N., Nie, W., Huang, X., Rusanen, A.,
1181 Ehn, M., Rissanen, M. P., Petäjä, T., Kulmala, M., and Boy, M.: Modelling studies of HOMs
1182 and their contributions to new particle formation and growth: comparison of boreal forest in
1183 Finland and a polluted environment in China, *Atmos. Chem. Phys.*, 18, 11779–11791,
1184 <https://doi.org/10.5194/acp-18-11779-2018>, 2018.

1185 Qiao, X., Yan, C., Li, X., Guo, Y., Yin, R., Deng, C., Li, C., Nie, W., Wang, M., Cai, R.,
1186 Huang, D., Wang, Z., Yao, L., Worsnop, D. R., Bianchi, F., Liu, Y., Donahue, N. M.,
1187 Kulmala, M., and Jiang, J.: Contribution of Atmospheric Oxygenated Organic Compounds to
1188 Particle Growth in an Urban Environment, *Environ. Sci. Technol.*,
1189 <https://doi.org/10.1021/acs.est.1c02095>, 2021.

1190 Qu, H., Wang, Y., Zhang, R., Liu, X., Huey, L. G., Sjostedt, S., Zeng, L., Lu, K., Wu, Y.,
1191 Shao, M., Hu, M., Tan, Z., Fuchs, H., Broch, S., Wahner, A., Zhu, T., and Zhang, Y.:
1192 Chemical Production of Oxygenated Volatile Organic Compounds Strongly Enhances
1193 Boundary-Layer Oxidation Chemistry and Ozone Production, *Environ. Sci. Technol.*, 55,
1194 13718–13727, <https://doi.org/10.1021/acs.est.1c04489>, 2021.

1195 Saunders, S. M., Jenkin, M. E., Derwent, R. G., and Pilling, M. J.: Protocol for the
1196 development of the Master Chemical Mechanism, MCM v3 (Part A): Tropospheric
1197 degradation of non-aromatic volatile organic compounds, *Atmos. Chem. Phys.*, 3, 161–180,
1198 <https://doi.org/10.5194/acp-3-161-2003>, 2003.

1199 Stolzenburg, D., Fischer, L., Vogel, A. L., Heinritzi, M., Schervish, M., Simon, M., Wagner,
1200 A. C., Dada, L., Ahonen, L. R., Amorim, A., Baccarini, A., Bauer, P. S., Baumgartner, B.,
1201 Bergen, A., Bianchi, F., Breitenlechner, M., Brilke, S., Mazon, S. B., Chen, D., Dias, A.,
1202 Draper, D. C., Duplissy, J., Haddad, I. El, Finkenzeller, H., Frege, C., Fuchs, C., Garmash, O.,
1203 Gordon, H., He, X., Helm, J., Hofbauer, V., Hoyle, C. R., Kim, C., Kirkby, J., Kontkanen, J.,
1204 Kürten, A., Lampilahti, J., Lawler, M., Lehtipalo, K., Leiminger, M., Mai, H., Mathot, S.,
1205 Mentler, B., Molteni, U., Nie, W., Nieminen, T., Nowak, J. B., Ojdanic, A., Onnela, A.,
1206 Passananti, M., Petäjä, T., Quéléver, L. L. J., Rissanen, M. P., Sarnela, N., Schallhart, S.,
1207 Tauber, C., Tomé, A., Wagner, R., Wang, M., Weitz, L., Wimmer, D., Xiao, M., Yan, C., Ye,
1208 P., Zha, Q., Baltensperger, U., Curtius, J., Dommen, J., Flagan, R. C., Kulmala, M., Smith, J.
1209 N., Worsnop, D. R., Hansel, A., Donahue, N. M., and Winkler, P. M.: Rapid growth of
1210 organic aerosol nanoparticles over a wide tropospheric temperature range, *Proc. Natl. Acad.*
1211 *Sci. U. S. A.*, 115, 9122–9127, <https://doi.org/10.1073/pnas.1807604115>, 2018.

1212 Tan, Z., Fuchs, H., Lu, K., Hofzumahaus, A., Bohn, B., Broch, S., Dong, H., Gomm, S.,
1213 Häsel, R., He, L., Holland, F., Li, X., Liu, Y., Lu, S., Rohrer, F., Shao, M., Wang, B.,
1214 Wang, M., Wu, Y., Zeng, L., Zhang, Y., Wahner, A., and Zhang, Y.: Radical chemistry at a
1215 rural site (Wangdu) in the North China Plain: Observation and model calculations of OH,
1216 HO₂ and RO₂ radicals, *Atmos. Chem. Phys.*, 17, 663–690, [https://doi.org/10.5194/acp-17-](https://doi.org/10.5194/acp-17-663-2017)
1217 [663-2017](https://doi.org/10.5194/acp-17-663-2017), 2017.

1218 Tan, Z., Rohrer, F., Lu, K., Ma, X., Bohn, B., Broch, S., Dong, H., Fuchs, H., Gkatzelis, G. I.,
1219 Hofzumahaus, A., Holland, F., Li, X., Liu, Y., Liu, Y., Novelli, A., Shao, M., Wang, H., Wu,
1220 Y., Zeng, L., Hu, M., Kiendler-Scharr, A., Wahner, A., and Zhang, Y.: Wintertime
1221 photochemistry in Beijing: Observations of RO_x radical concentrations in the North China
1222 Plain during the BEST-ONE campaign, *Atmos. Chem. Phys.*, [https://doi.org/10.5194/acp-18-](https://doi.org/10.5194/acp-18-12391-2018)
1223 [12391-2018](https://doi.org/10.5194/acp-18-12391-2018), 2018.

1224 Tan, Z., Lu, K., Jiang, M., Su, R., Wang, H., Lou, S., Fu, Q., Zhai, C., Tan, Q., Yue, D.,
1225 Chen, D., Wang, Z., Xie, S., Zeng, L., and Zhang, Y.: Daytime atmospheric oxidation
1226 capacity in four Chinese megacities during the photochemically polluted season: A case study
1227 based on box model simulation, *Atmos. Chem. Phys.*, 19, 3493–3513,
1228 <https://doi.org/10.5194/acp-19-3493-2019>, 2019.

1229 Tröstl, J., Chuang, W. K., Gordon, H., Heinritzi, M., Yan, C., Molteni, U., Ahlm, L., Frege,
1230 C., Bianchi, F., Wagner, R., Simon, M., Lehtipalo, K., Williamson, C., Craven, J. S.,
1231 Duplissy, J., Adamov, A., Almeida, J., Bernhammer, A. K., Breitenlechner, M., Brilke, S.,
1232 Dias, A., Ehrhart, S., Flagan, R. C., Franchin, A., Fuchs, C., Guida, R., Gysel, M., Hansel, A.,
1233 Hoyle, C. R., Jokinen, T., Junninen, H., Kangasluoma, J., Keskinen, H., Kim, J., Krapf, M.,
1234 Kürten, A., Laaksonen, A., Lawler, M., Leiminger, M., Mathot, S., Möhler, O., Nieminen, T.,
1235 Onnela, A., Petäjä, T., Piel, F. M., Miettinen, P., Rissanen, M. P., Rondo, L., Sarnela, N.,
1236 Schobesberger, S., Sengupta, K., Sipilä, M., Smith, J. N., Steiner, G., Tomè, A., Virtanen, A.,
1237 Wagner, A. C., Weingartner, E., Wimmer, D., Winkler, P. M., Ye, P., Carslaw, K. S., Curtius,
1238 J., Dommen, J., Kirkby, J., Kulmala, M., Riipinen, I., Worsnop, D. R., Donahue, N. M., and
1239 Baltensperger, U.: The role of low-volatility organic compounds in initial particle growth in
1240 the atmosphere, *Nature*, 533, 527–531, <https://doi.org/10.1038/nature18271>, 2016.
1241 Tsiligiannis, E., Hammes, J., Salvador, C. M., Mentel, T. F., and Hallquist, M.: Effect of NO_x
1242 on 1,3,5-trimethylbenzene (TMB) oxidation product distribution and particle formation,
1243 *Atmos. Chem. Phys.*, 19, 15073–15086, <https://doi.org/10.5194/acp-19-15073-2019>, 2019.
1244 Vereecken, L.: Reaction Mechanisms for the Atmospheric Oxidation of Monocyclic Aromatic
1245 Compounds, *Adv. Atmos. Chem.*, 377–527, https://doi.org/10.1142/9789813271838_0006,
1246 2019.
1247 Wang, L., Wu, R., and Xu, C.: Atmospheric oxidation mechanism of benzene. Fates of alkoxy
1248 radical intermediates and revised mechanism, *J. Phys. Chem. A*, 117, 14163–14168,
1249 <https://doi.org/10.1021/jp4101762>, 2013.
1250 Wang, M., Chen, D., Xiao, M., Ye, Q., Stolzenburg, D., Hofbauer, V., Ye, P., Vogel, A. L.,
1251 Mauldin, R. L., Amorim, A., Baccarini, A., Baumgartner, B., Brilke, S., Dada, L., Dias, A.,
1252 Duplissy, J., Finkenzeller, H., Garmash, O., He, X. C., Hoyle, C. R., Kim, C., Kuvshinov, A.,
1253 Lehtipalo, K., Fischer, L., Molteni, U., Petäjä, T., Pospisilova, V., Quéléver, L. L. J.,
1254 Rissanen, M., Simon, M., Tauber, C., Tomé, A., Wagner, A. C., Weitz, L., Volkamer, R.,
1255 Winkler, P. M., Kirkby, J., Worsnop, D. R., Kulmala, M., Baltensperger, U., Dommen, J., El-
1256 Haddad, I., and Donahue, N. M.: Photo-oxidation of Aromatic Hydrocarbons Produces Low-
1257 Volatility Organic Compounds, *Environ. Sci. Technol.*, 54, 7911–7921,
1258 <https://doi.org/10.1021/acs.est.0c02100>, 2020a.
1259 Wang, S., Wu, R., Berndt, T., Ehn, M., and Wang, L.: Formation of Highly Oxidized Radicals
1260 and Multifunctional Products from the Atmospheric Oxidation of Alkylbenzenes, *Environ.*
1261 *Sci. Technol.*, 51, 8442–8449, <https://doi.org/10.1021/acs.est.7b02374>, 2017.
1262 Wang, W., Yuan, B., Peng, Y., Su, H., Cheng, Y., and Yang, S.: Direct observations indicate
1263 photodegradable oxygenated VOCs as larger contributors to radicals and ozone production in
1264 the atmosphere, *Atmos. Chem. Phys.*, 1–28, 2022.
1265 Wang, Y., Mehra, A., Krechmer, J. E., Yang, G., Hu, X., Lu, Y., Lambe, A., Canagaratna, M.,
1266 Chen, J., Worsnop, D., Coe, H., and Wang, L.: Oxygenated products formed from OH-
1267 initiated reactions of trimethylbenzene: autoxidation and accretion, *Atmos. Chem. Phys.*, 20,
1268 9563–9579, <https://doi.org/10.5194/acp-20-9563-2020>, 2020b.
1269 Whalley, L. K., Slater, E. J., Woodward-Massey, R., Ye, C., Lee, J. D., Squires, F., Hopkins,
1270 J. R., Dunmore, R. E., Shaw, M., Hamilton, J. F., Lewis, A. C., Mehra, A., Worrall, S. D.,
1271 Bacak, A., Bannan, T. J., Coe, H., Percival, C. J., Ouyang, B., Jones, R. L., Crilley, L. R.,
1272 Kramer, L. J., Bloss, W. J., Vu, T., Kotthaus, S., Grimmond, S., Sun, Y., Xu, W., Yue, S.,

1273 Ren, L., Joe, W., Nicholas Hewitt, C., Wang, X., Fu, P., and Heard, D. E.: Evaluating the
1274 sensitivity of radical chemistry and ozone formation to ambient VOCs and NO_x in Beijing,
1275 *Atmos. Chem. Phys.*, 21, 2125–2147, <https://doi.org/10.5194/acp-21-2125-2021>, 2021.
1276 Xu, L., Møller, K. H., Crounse, J. D., Kjaergaard, H. G., and Wennberg, P. O.: New insights
1277 into the radical chemistry and product distribution in the OH-initiated oxidation of benzene,
1278 *Environ. Sci. Technol.*, 54, 13467–13477, <https://doi.org/10.1021/acs.est.0c04780>, 2020.
1279 Yan, C., Kocevskaja, S., and Krasnoperov, L. N.: Kinetics of the Reaction of CH₃O₂ Radicals
1280 with OH Studied over the 292–526 K Temperature Range, *J. Phys. Chem. A*, 120, 6111–6121,
1281 <https://doi.org/10.1021/acs.jpca.6b04213>, 2016.
1282 Yang, C., Yao, N., Xu, L., Chen, G., Wang, Y., Fan, X., Zhou, P., Clusius, P., Tham, Y. J.,
1283 Lin, Z., Chen, Y., Li, M., Hong, Y., and Chen, J.: Molecular Composition of Anthropogenic
1284 Oxygenated Organic Molecules and Their Contribution to Organic Aerosol in a Coastal City,
1285 *Environ. Sci. Technol.*, 57, 15956–15967, <https://doi.org/10.1021/acs.est.3c03244>, 2023.
1286 Yao, L., Garmash, O., Bianchi, F., Zheng, J., Yan, C., Kontkanen, J., Junninen, H., Mazon, S.
1287 B., Ehn, M., Paasonen, P., Sipilä, M., Wang, M., Wang, X., Xiao, S., Chen, H., Lu, Y.,
1288 Zhang, B., Wang, D., Fu, Q., Geng, F., Li, L., Wang, H., Qiao, L., Yang, X., Chen, J.,
1289 Kerminen, V.-M., Petäjä, T., Worsnop, D. R., Kulmala, M., and Wang, L.: Atmospheric new
1290 particle formation from sulfuric acid and amines in a Chinese megacity, *Science* (80-.), 361,
1291 278–281, <https://doi.org/10.1126/science.aao4839>, 2018.
1292 Yuan, B., Chen, W., Shao, M., Wang, M., Lu, S., Wang, B., Liu, Y., Chang, C. C., and Wang,
1293 B.: Measurements of ambient hydrocarbons and carbonyls in the Pearl River Delta (PRD),
1294 China, *Atmos. Res.*, 116, 93–104, <https://doi.org/10.1016/j.atmosres.2012.03.006>, 2012.
1295 Zaytsev, A., Koss, A. R., Breitenlechner, M., Krechmer, J. E., Nihill, K. J., Lim, C. Y., Rowe,
1296 J. C., Cox, J. L., Moss, J., Roscioli, J. R., Canagaratna, M. R., Worsnop, D. R., Kroll, J. H.,
1297 and Keutsch, F. N.: Mechanistic study of the formation of ring-retaining and ring-opening
1298 products from the oxidation of aromatic compounds under urban atmospheric conditions,
1299 *Atmos. Chem. Phys.*, 19, 15117–15129, <https://doi.org/10.5194/acp-19-15117-2019>, 2019.
1300 Zhao, Y., Thornton, J. A., and Pye, H. O. T.: Quantitative constraints on autoxidation and
1301 dimer formation from direct probing of monoterpene-derived peroxy radical chemistry, *Proc.*
1302 *Natl. Acad. Sci.*, 115, 12142–12147, <https://doi.org/10.1073/pnas.1812147115>, 2018.
1303